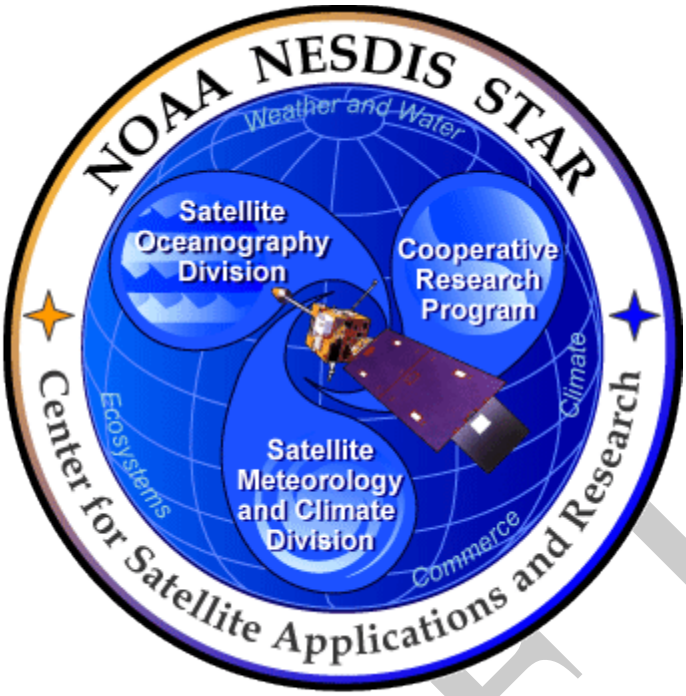

NOAA NESDIS
CENTER for SATELLITE APPLICATIONS and RESEARCH

Enterprise Algorithm Theoretical Basis Document For Volcanic Ash (Detection and Height)

Michael Pavolonis, NOAA/NESDIS/STAR
Justin Sieglaff, UW-CIMSS

Version 4.0
December 18, 2015

TABLE OF CONTENTS

LIST OF FIGURES

LIST OF TABLES

LIST OF ACRONYMS

ABI – Advanced Baseline Imager
ABI-VAA – Advanced Baseline Imager Volcanic Ash Algorithm
AC – Above Cloud
AIADD – Algorithm Interface and Ancillary Data Description
ATBD – Algorithm Theoretical Basis Document
AWG – Algorithm Working Group
CALIOP – Cloud-Aerosol Lidar with Orthogonal Polarization
CALIPSO – Cloud-Aerosol Lidar and Infrared Pathfinder Satellite Observation
CDF – Cumulative Distribution Function
CONUS – Continental United States
ECMWF – European Centre for Medium-Range Weather Forecasts
EOS – Earth Observing System
ESA – European Space Agency
F&PS – Functional & Performance Specification
GOES – Geostationary Operational Environmental Satellite
JPSS – Joint Polar Satellite System
LRC – Local Radiative Center
MODIS – Moderate Resolution Imaging Spectroradiometer
NASA – National Aeronautics and Space Agency
NESDIS – National Environmental Satellite, Data, and Information Service
NOAA – National Oceanic and Atmospheric Administration
NWP – Numerical Weather Prediction
POES – Polar Operational Environmental Satellite
SEVIRI – Spinning Enhanced Visible and Infrared Imager
SSEC – Space Science and Engineering Center
STAR – Center for Satellite Applications and Research
TOA – Top of Atmosphere
TRR – Test Readiness Review
UTC – Coordinated Universal Time
VIIRS – Visible Infrared Imaging Radiometer Suite

ABSTRACT

The volcanic ash algorithm theoretical basis document (ATBD) provides a high level description of the physical basis for the estimation of cloud height and mass loading (mass per unit area) of volcanic ash clouds observed by the Advanced Baseline Imager (ABI) flown on the GOES-R series of NOAA geostationary meteorological satellites. This ATBD is also valid for the JPSS-VIIRS volcanic ash algorithm. Much of the GOES-R ABI algorithm content is directly applicable to the JPSS-VIIRS implementation, however special subsections and inline comments are provided where the two algorithms may differ due to fewer spectral channels available from VIIRS. The generation of these baseline products relies on the ability to determine which pixels potentially contain volcanic ash, so the procedure for determining if there is a high confidence of a given pixel containing volcanic ash is also described.

Pixels that potentially contain volcanic ash are identified using a series of spectral and spatial tests. The detection algorithm utilizes ABI channels 10 (7.4 μm), 11 (8.5 μm), 14 (11 μm), and 15 (12 μm) (VIIRS channels 14 (8.5 μm), 15 (11 μm), and 16 (12 μm). In lieu of brightness temperature differences, effective absorption optical depth ratios are mainly used in the spectral tests. Effective absorption optical depth ratios allow for improved sensitivity to cloud microphysics, especially for optically thin clouds. An optimal estimation technique is then applied to all pixels that potentially contain ash in order to estimate the height and mass loading of ash clouds. This retrieval technique utilizes ABI channels 14 (11 μm), 15 (12 μm), and 16 (13.3 μm) (VIIRS channels 15 (11 μm) and 16 (12 μm). While these are difficult products to validate, comparisons to spaceborne lidar indicate that this approach is meeting the accuracy requirements.

1.1 Purpose of This Document

The volcanic ash algorithm theoretical basis document (ATBD) provides a high level description of the physical basis for the estimation of cloud height and mass loading (mass per unit area) of volcanic ash clouds observed by the Advanced Baseline Imager (ABI) flown on the GOES-R series of NOAA geostationary meteorological satellites. The generation of these baseline products relies on the ability to determine which pixels potentially contain volcanic ash, so the procedure for determining if there is a high confidence of a given pixel containing volcanic ash is also described.

This document was modified in late 2015 to also include documentation for the JPSS/VIIRS implementation of the GOES-R ABI Volcanic Ash algorithms. The original document (GOES-R ABI ATBD) is generally applicable to JPSS/VIIRS. Given the more limited set of spectral channels available from VIIRS, some small modifications were necessary. In these scenarios, either special subsections have been added to the ATBD describing how the JPSS/VIIRS volcanic ash algorithm(s) differ from the GOES-R ABI implementation or inline comments are provided unique toward JPSS/VIIRS implementation.

1.2 Who Should Use This Document

The intended user of this document are those interested in understanding the physical basis of the algorithms and how to use the output of this algorithm. This document also provides information useful to anyone maintaining or modifying the original algorithm.

1.3 Inside Each Section

This document is broken down into the following main sections.

- **System Overview**: Provides relevant details of the ABI and provides a brief description of the products generated by the algorithm.

- **Algorithm Description**: Provides all the detailed description of the algorithm including its physical basis, its input and its output.

- **Test Data Sets and Outputs:** Provides a detailed description of the data sets used to develop and test the GOES-R ABI algorithm and describes the algorithm output.

- **Practical Considerations:** Provides a description of algorithm programming and quality control considerations.

- **Assumptions and Limitations**: Provides an overview of the current limitations of the approach and gives the plan for overcoming these limitations with further algorithm development.

1.4 Related Documents

- GOES-R Functional & Performance Specification Document (F&PS)
- GOES-R ABI Volcanic Ash Product Validation Plan Document
- Algorithm Interface and Ancillary Data Description (AIADD) Document

1.5 Revision History

- 9/30/2008 - Version 0.1 of this document was created by Michael J Pavolonis (NOAA/NESDIS/STAR) and Justin Sieglaff (University of Wisconsin – Madison). Version 0.1 represents the first draft of this document.

- 6/30/2009 – Version 1.0 of this document was created by Michael J Pavolonis (NOAA/NESDIS/STAR) and Justin Sieglaff (University of Wisconsin – Madison). In this revision, Version 0.1 was revised to meet 80% delivery standards.

- 6/30/2010 – Version 2.0 of this document was created by Michael J Pavolonis (NOAA/NESDIS/STAR) and Justin Sieglaff (University of Wisconsin – Madison). In this revision, Version 1.0 was revised to meet 100% delivery standards.

- 9/15/2010 – Version 2.1 of this document was updated by Michael J Pavolonis (NOAA/NESDIS/STAR) and Justin Sieglaff (University of Wisconsin – Madison). In this revision, Version 2.0 was revised to meet 100% delivery standards.

- 7/9/2012 – Version 3.0 of this document was updated by Michael J Pavolonis (NOAA/NESDIS/STAR) and Justin Sieglaff (University of Wisconsin – Madison). In this revision, Version 2.1 was revised to meet 100% delivery standards and update minor errors.

- 12/18/2015 – Version 4.0 of this document was updated by Michael J Pavolonis (NOAA/NESDIS/STAR) and Justin Sieglaff (University of Wisconsin – Madison). In this revision, Version 3.0 was revised to include subsections and content related to the JPSS/VIIRS implementation of the GOES-R algorithm.

2 OBSERVING SYSTEM OVERVIEW

This section will describe the products generated by the ABI Volcanic Ash Algorithm (ABI-VAA) and the requirements it places on the sensor.

2.1 Products Generated

The ABI-VAA is responsible for producing an ash cloud height and ash cloud mass loading (mass per unit area) for all ABI pixels that potentially contain volcanic ash. The ABI-VAA also produces several quality flags.

The ABI volcanic ash products are intended to locate volcanic ash clouds and to initialize and validate ash dispersion models.

2.1.1 Product Requirements

The F&PS spatial, temporal, and accuracy requirements for the GOES-R volcanic ash products are shown below in Table 1.

Name	User & Priority	Geographic Coverage	Vertical Res.	Horiz. Res.	Mapping Accuracy	Msmnt. Rang	Msmnt. Accuracy	Refresh Rate/Coverage Time Option (Mode 3)	Refresh Rate Option (Mode 4)	Data Latency	Long-Term	Product Measurement Precision
Volcanic Ash: detection and height	GOES-R	FD	3 km (top height)	2 km	1 km	0-50 tons/km^2	2 tons/km^2	15 min	15 min	430 sec	TBD	2.5 tons/km^2

Name	User & Priority	Geographic Coverage	Tempral Coverage Qualifiers	Product Extend Qualifiers	Cloud Cover Conditions Qualifiers	Product Statistics Qualifier
Volcanic Ash: detection and height	GOES-R	FD	Day and night	Quantitative out to at least 60 degrees LZA and qualitative beyond	Clear conditions down to feature of interest associated with threshold accuracy	Over volcanic ash cases

Table 1: The GOES-R volcanic ash detection and height requirements. The Geographic Coverage definitions are: M=Mesoscale, C=CONUS, and FD=Full Disk.

2.1.1.1 Product Requirements – JPSS/VIIRS

This subsection modifies the parent subsection to reflect product requirements for JPSS/VIIRS-VAA.

Name	User & Priority	Geographic Coverage	Vertical Res.	Horiz. Res.	Msmnt. Rang	Msmnt. Accuracy	Refresh Rate/Coverage Time Option (Mode 3)	Refresh Rate	Data Latency	Product Measurement Precision
Volcanic Ash: detection and height	VIIIRS	Global	3 km (top height)	750 m	0-50 tons/ km^2	2 $tons/km^2$	15 min	90 min	30 min	2.5 $tons/km^2$

Name	User & Priority	Geographic Coverage	Temporal Coverage Qualifiers	Cloud Cover Conditions Qualifiers	Product Statistics Qualifier
Volcanic Ash: detection and height	VIIIRS	Global	Day and night	Clear conditions down to feature of interest associated with threshold accuracy	Over volcanic ash cases

Table 2: The JPSS volcanic ash detection and height requirements.

2.2 Instrument Characteristics

The ABI volcanic ash height and mass loading retrieval will be applied to each pixel that potentially contains volcanic ash as determined by the ash detection component of the algorithm. Table 3 summarizes the current channels use by the ABI-VAA.

Channel Number	*Wavelength (μm)*	*Used in ABI-VAA*
1	0.47	
2	0.64	
3	0.86	
4	1.38	
5	1.61	
6	2.26	

7	3.9	
8	6.15	
9	7.0	
10	7.4	✓
11	8.5	✓
12	9.7	
13	10.35	
14	11.2	✓
15	12.3	✓
16	13.3	✓

Table 3: Channel numbers and wavelengths for the ABI

The ABI-VAA relies on infrared radiances to avoid day/night/terminator discontinuities. Channel 16 provides the needed sensitivity to cloud height for optically thin mid and high level ash clouds while channels 10, 11 and 14-15 provide the needed sensitivity to cloud microphysics (including composition).

The performance of the ABI-VAA is sensitive to any imagery artifacts or instrument noise. The ABI-VAA expects all observations to be in the form of navigated and calibrated radiances and brightness temperatures. This is critical because the volcanic ash mask compares the observed values to those from a forward radiative transfer model. The channel specifications are given in the F&PS section 3.4.2.1.4.0. We are assuming the performance outlined in this section during our development efforts.

2.2.1 Instrument Characteristics – JPSS/VIIRS

This subsection modifies the parent subsection to reflect the JPSS/VIIRS channels. The JPSS/VIIRS volcanic ash height and mass loading retrieval will be applied to each pixel that potentially contains volcanic ash as determined by the ash detection component of the algorithm. Table 4 summarizes the current channels use by the JPSS/VIIRS-VAA.

Channel Number	*Wavelength (μm)*	*Used in VIIRS-VAA*
M1	0.412	
M2	0.445	
M3	0.488	
M4	0.555	
M5	0.672	
M6	0.746	
M7	0.865	
M8	1.240	
M9	1.378	
M10	1.61	
M11	2.25	

M12	3.7	
M13	4.05	
M14	8.55	✓
M15	10.763	✓
M16	12.013	✓

Table 4: Channel numbers and wavelengths for the VIIRS

The VIIRS-VAA relies on infrared radiances to avoid day/night/terminator discontinuities. Channels M14-16 provide the needed sensitivity to cloud microphysics (including composition) and channels M15 and M16 provide sensitivity to cloud height.

3 ALGORITHM DESCRIPTION

Below is a complete description of the algorithm at the current level of maturity (which will improve with each revision).

3.1 Algorithm Overview

Given the importance of monitoring volcanic ash for aviation interests, health interests, and climate, the ABI-VAA serves a critical role in the GOES-R ABI processing system. Information pertaining to volcanic ash is needed on a very timely basis. As such, latency was a large concern in the development of the ABI-VAA. Given advances made in fast radiative transfer modeling, a state-of-the-art algorithm can be implemented without risking latency issues. The ash cloud height/mass loading retrieval utilizes the same general retrieval procedure as the ABI cloud top height algorithm. Some of the details within the retrieval procedure were modified to accommodate volcanic ash clouds, which, spectrally, behave quite a bit different than meteorological clouds. Given any type of cloud that produces a discernable signal in the infrared, the height/mass loading retrieval will produce an answer. Thus, the application of the retrieval needs to be restricted to pixels that potentially contain volcanic ash clouds. To ensure that this is the case, an ash detection algorithm is applied to all pixels prior to performing the retrieval. The ash detection simply determines the likelihood that volcanic ash is present. Volcanic ash detection is a very specialized application, so one cannot expect the cloud mask to provide this information. It is important to note that the ash detection algorithm often detects non-volcanic dust. The F&PS product statistics qualifier, "over volcanic ash cases," allows the detection algorithm to have false alarms, like non-volcanic dust.

The ABI-VAA derives the following ABI cloud products listed in the F&PS.

- Ash cloud height [km]
- Ash mass loading [tons/km^2]

Both of these products are derived at the pixel level for all pixels that potentially contain volcanic ash.

In addition, the ABI-VAA derives the following products that are not included in F&PS.

- Quality Flags (including the confidence of volcanic ash being present in a given pixel) (for ash detection and ash retrieval algorithms) (defined in section 3.4.5)
- Product Quality Information (for ash detection and ash retrieval algorithms) (defined in section 3.4.5)
- Metadata (defined in section 3.4.5)

3.2 Processing Outline

As described earlier, the ash height and mass loading retrieval requires *a priori* knowledge of which pixels contain volcanic ash. Thus, prior to calling the ash retrieval algorithm, an ash detection algorithm must be applied to determine which pixels likely contain volcanic ash (based upon ash confindence). Given this requirement, the algorithm processing precedence is as follows: ash detection routine --> ash retrieval routine. Both ash routines require multiple scan lines of ABI data due to the spatial analysis that is applied within each. Complete scan line segments should consist of at least the minimum number of scan lines required by the Gradient Filter, which is described in detail in the Algorithm Interface and Ancillary Data Description (AIADD) Document. While overlap between adjacent scan line segments is beneficial, scan line overlap was not used in the development and validation of this algorithm. The processing outline of the ash height and mass loading retrieval is summarized in the figure below.

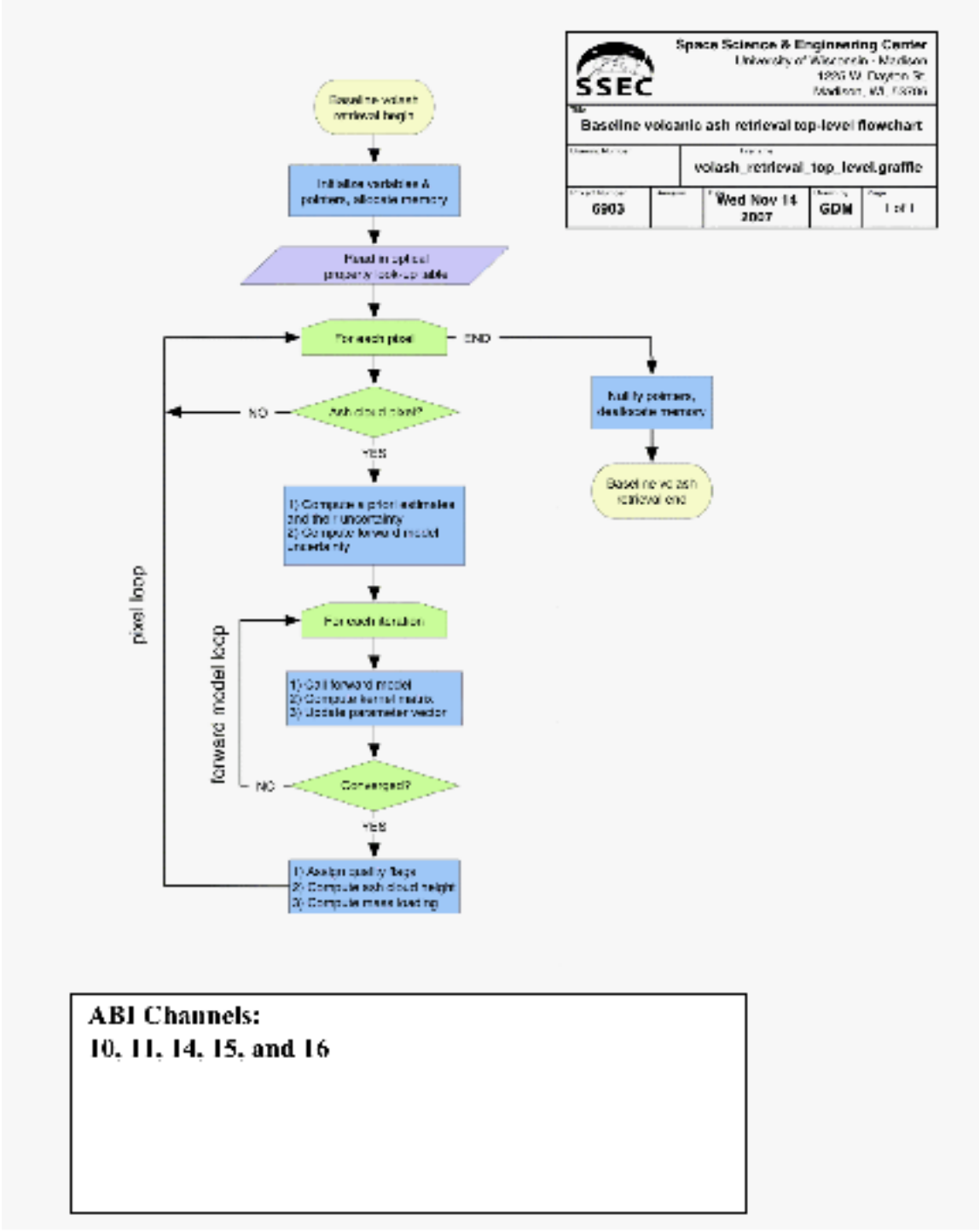

Figure 1: High Level Flowchart of the ABI_VAA illustrating the main processing sections.

3.3 Algorithm Input

This section describes the input needed to process the ABI-VAA. While the ABI-VAA operates on a pixel-by-pixel basis, surrounding pixels are needed for spatial analysis. Therefore, the ABI-VAA must have access to a group of pixels. In its current configuration, we run the ABI-VAA on segments comprised of 200 scan-lines. The minimum scan line segment size required to implement the ABI-VAA is driven by the minimum number of scan lines required to fully utilize the gradient filter routine (see AIADD Document for more details). The following sections describe the actual input needed to run the ABI-VAA.

3.3.1 Primary Sensor Data

The list below contains the primary sensor data currently used by the ABI-VAA. By primary sensor data, we mean information that is derived solely from the ABI observations and geolocation information.

- Calibrated radiances for ABI channels 10 (7.4 μm), 11 (8.5 μm), 14 (11 μm), 15 (12 μm), and 16 (13.3 μm).
- Calibrated brightness temperatures for ABI channels 14 (11 μm), 15 (12 μm), and 16 (13.3 μm).
- Sensor viewing zenith angle (degrees)
- L1b quality information from calibration for ABI channels 10, 11, 14, 15, and 16
- Space mask (is the pixel geolocated on the surface of the Earth?)

3.3.1.1 Primary Sensor Data – JPSS/VIIRS

This section modifies the parent subsection to reflect JPSS/VIIRS channels used by the VIIRS-VAA.

- Calibrated radiances for VIIRS channels 14 (8.5 μm), 15 (11 μm), and 16 (12 μm).
- Calibrated brightness temperatures for VIIRS channels 14 (11 μm) and 15 (12 μm).
- Sensor viewing zenith angle (degrees)
- L1b quality information from calibration for VIIRS channels 14, 15, and 16
- Space mask (is the pixel geolocated on the surface of the Earth?)

3.3.2 Ancillary Data

The following data lists and briefly describes the ancillary data required to run the ABI-VAA. By ancillary data, we mean data that requires information not included in the ABI observations or geolocation data.

- **Land cover / Surface type**
  A global land cover classification collection created by The University of Maryland Department of Geography (Hansen et al. 1998). Imagery from the AVHRR satellites acquired between 1981 and 1994 were used to distinguish fourteen land cover classes (http://glcf.umiacs.umd.edu/data/landcover/). This product is available at 1 km pixel resolution. See the AIADD Document for additional information.

- **Surface emissivity of ABI channels 14 and 15**
- A global database of monthly mean infrared land surface emissivity is required for ABI channels 14 and 15. The ABI-VAA utilizes surface emissivity derived using the Moderate Resolution Imaging Spectroradiometer (MODIS). Emissivity is available globally at ten generic wavelengths (3.6, 4.3, 5.0, 5.8, 7.6, 8.3, 9.3, 10.8, 12.1, and 14.3 microns) with 0.05 degree spatial resolution (Seemann et al. 2008). The ten wavelengths serve as anchor points in the linear interpolation to any wavelength between 3.6 and 14.3 microns. The monthly emissivities have been integrated over the ABI spectral response functions to match the ABI channels. This data set and the procedure for spectrally and spatially mapping it to the ABI are described in detail in Seemann et al. 2008 and the AIADD Document.

- **Profiles of pressure, temperature, and height**
  The calculation of cloud emissivity requires profiles of pressure, temperature, and height from a global Numerical Weather Prediction (NWP) model. In addition, knowledge of the location of the surface and tropopause levels is required. While six-hour forecasts were used in the development of the ABI-VAA, and, as such, are recommended, any forecast in the 0 to 24 hour range is acceptable. Details concerning the NWP data can be found in the AIADD Document.

3.3.3 Radiative Transfer Models

The following lists and briefly describes the data that must be calculated by a radiative transfer model or derived prior to running the ABI-VAA. See the AIADD Document for a more detailed description.

- **Black cloud radiance profiles for channels 10, 11, 14, 15 and 16**
  The ABI-VAA requires the radiance emitted upward by a black body surface and transmitted through a non-cloudy atmosphere, with gaseous absorption, to the top of the atmosphere as a function of the atmospheric level of the black surface. The black cloud radiance is computed as a function of NWP grid cells and viewing angle (it is not computed at the pixel resolution), as described in detail in the AIADD Document.

- **Clear sky atmospheric transmittance profiles for channels 14, 15 and 16**

The ABI-VAA requires a vertical profile of the clear sky atmospheric transmittance (transmittance from a given level to the top-of-atmosphere). The clear sky atmospheric transmittance is computed as a function of NWP grid cells and viewing angle (it is not computed at the pixel resolution), as described in detail in the AIADD Document.

- **Top-of-atmosphere clear-sky radiance estimates of channels 10, 11, 14, 15 and 16**
  The ABI-VAA forward model requires knowledge of the radiance ABI would sense under clear-sky conditions at each pixel.

3.3.3.1 Radiative Transfer Models – JPSS/VIIRS

This subsection modifies the parent subsection to reflect JPSS/VIIRS channel subset. The following lists and briefly describes the data that must be calculated by a radiative transfer model or derived prior to running the VIIRS-VAA. See the AIADD Document for a more detailed description.

- **Black cloud radiance profiles for VIIRS channels 14, 15 and 16**
  The VIIRS-VAA requires the radiance emitted upward by a black body surface and transmitted through a non-cloudy atmosphere, with gaseous absorption, to the top of the atmosphere as a function of the atmospheric level of the black surface. The black cloud radiance is computed as a function of NWP grid cells and viewing angle (it is not computed at the pixel resolution), as described in detail in the AIADD Document.

- **Clear sky atmospheric transmittance profiles for VIIRS channels 15 and 16**
  The VIIRS-VAA requires a vertical profile of the clear sky atmospheric transmittance (transmittance from a given level to the top-of-atmosphere). The clear sky atmospheric transmittance is computed as a function of NWP grid cells and viewing angle (it is not computed at the pixel resolution), as described in detail in the AIADD Document.

- **Top-of-atmosphere clear-sky radiance estimates of VIIRS channels 14, 15 and 16**
  The VIIRS-VAA forward model requires knowledge of the radiance VIIRS would sense under clear-sky conditions at each pixel.

3.4 Theoretical Description

Important: *These following sub-sections are divided into two parts, one describing the volcanic ash detection methodology, and one describing the volcanic ash height and mass loading retrieval. Some of the physical concepts described in each part will overlap. For the sake of clarity, each part contains a complete description, which results in some redundancy.*

The volcanic ash detection methodology described in this section is based on the physical concepts described in Pavolonis (2010a) and Pavolonis (2010b). The general volcanic ash height and mass loading retrieval methodology is based on the work of Heidinger and Pavolonis (2009).

Both the volcanic ash detection and volcanic ash physical property retrieval sections have quality indicators associated with the algorithm. Most tests in subsequent sections have their results stored in QF and PQI flags. These flags are described in detail in the 'Algorithm Output' (section 3.4.5) but are also defined in the following subsections.

3.4.1 Physics of the Problem – Volcanic Ash Detection

The volcanic ash detection method utilizes ABI Channels 10, 11, 14, and 15 (VIIRS channels 14, 15, and 16). These channels have an approximate central wavelength of 7.4, 8.5, 11, and 12 μm (8.5, 11, and 12 μm), respectively. These central wavelengths will be referred to rather than the ABI channel numbers throughout the "Theoretical Description." The spectral sensitivity to cloud composition is perhaps best understood by examining the imaginary index of refraction, m_i, as a function of wavelength. The imaginary index of refraction is often directly proportional to absorption/emission strength for a given particle composition, in that larger values are indicative of stronger absorption of radiation at a particular wavelength. However, absorption due to photon tunneling, which is proportional to the real index of refraction, can also contribute to the observed spectral absorption under certain circumstances (Mitchell, 2000), but for simplicity, only absorption by the geometrical cross section, which is captured by the imaginary index of refraction, is discussed here. Figure 2 shows m_i for liquid water (Downing and Williams, 1975), ice (Warren and Brandt, 2008), volcanic rock (andesite) (Pollack et al., 1973), and non-volcanic dust (kaolinite) (Roush et al., 1991). While the exact composition, and hence the m_i, of volcanic ash and dust vary depending on the source, andesite and kaolinite were chosen since both minerals exhibit the often exploited "reverse absorption" signature (e.g. Prata, 1989). The "reverse absorption" signature is responsible for the sometimes-observed negative 11 – 12 μm brightness temperature difference associated with volcanic ash and dust.

The m_i can be interpreted as follows. In Figure 2, one sees that around 10 - 11 μm volcanic rock absorbs more strongly than liquid water or ice, while near 12 – 13.5 μm the opposite is true. Thus, all else being equal, the measured brightness temperature by an 12 μm channel will exceed the measured brightness temperature by an 11 μm channel for a volcanic ash cloud, with the opposite being true for a meteorological cloud (e.g. a cloud composed of liquid water and/or ice). The previous statement is only accurate if the meteorological cloud and volcanic ash cloud have the same particle concentrations at the same vertical levels in the same atmosphere, and have the same particle size and shape distribution. That is what is meant by "all else being equal." While Figure 2 is insightful, it can also be deceiving if not interpreted correctly. For example, it is possible that a scene with a meteorological cloud in one type of atmosphere (e.g. contintental mid-

latitude) may exhibit the same measured spectral radiance as a scene with an ash cloud in another type of atmosphere (e.g. maritime tropical).

In order to maximize the sensitivity to cloud composition, the information contained in Figure 2 must be extracted from the measured radiances as best as possible. One way of doing this is to account for the background conditions (e.g. surface temperature, surface emissivity, atmospheric temperature, and atmospheric water vapor) of a given scene in an effort to isolate the cloud microphysical signal. This is difficult to accomplish with traditional brightness temperatures and brightness temperature differences. In the following section, we derive a data space that accounts for the background conditions.

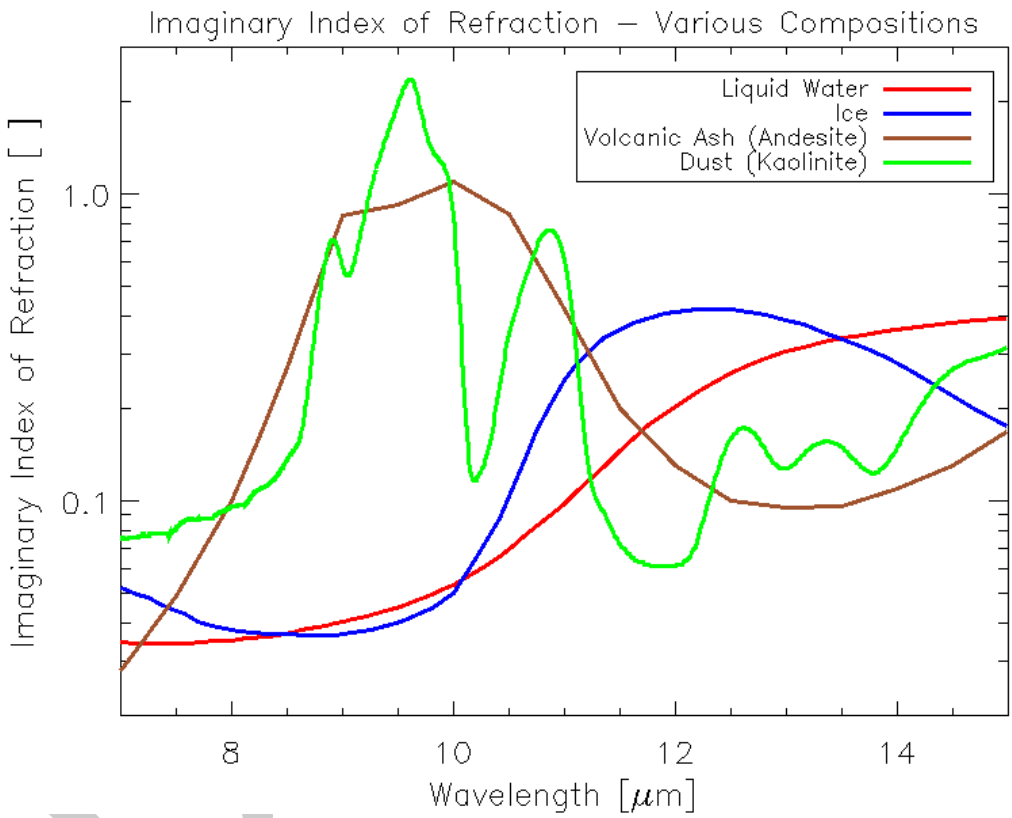

Figure 2: The imaginary index of refraction for liquid water (red), ice (blue), andesite (brown), and kaolinite (green) is shown as a function of wavelength.

3.4.1.1 Infrared Radiative Transfer used in Ash Detection

Assuming a satellite viewing perspective (e.g. upwelling radiation), a fully cloudy field of view, a non-scattering atmosphere (no molecular scattering), and a negligible contribution from downwelling cloud emission or molecular emission that is reflected by the surface and transmitted to the top of troposphere (Zhang and Menzel (2002) showed that this term is very small at infrared wavelengths), the cloudy radiative transfer

equation for a given infrared channel or wavelength can be written as in Equation 1 (e.g. Heidinger and Pavolonis, 2009).

$$R_{obs}(\lambda) = \varepsilon(\lambda)R_{ac}(\lambda) + t_{ac}(\lambda)\varepsilon(\lambda)B(\lambda, T_{eff}) + R_{clr}(\lambda)(1-\varepsilon(\lambda)) \quad \text{(Eq. 1)}$$

In Equation 1, λ is wavelength, R_{obs} is the observed radiance, R_{clr} is the clear sky radiance. R_{ac} and t_{ac} are the above cloud upwelling atmospheric radiance and transmittance, respectively. B is the Planck Function, and T_{eff} is the effective cloud temperature. The estimation of the clear sky radiance and transmittance will be explained later on in this section. The effective cloud emissivity (Cox, 1976) is given by ε. To avoid using additional symbols, the angular dependence is simply implied.

Equation 1 can readily be solved for the effective cloud emissivity as follows:

$$\varepsilon(\lambda) = \frac{R_{obs}(\lambda) - R_{clr}(\lambda)}{[B(\lambda, T_{eff})t_{ac}(\lambda) + R_{ac}(\lambda)] - R_{clr}(\lambda)} \quad \text{(Eq. 2)}$$

In Equation 2, the term in brackets in the denominator is the blackbody cloud radiance that is transmitted to the top of atmosphere (TOA) plus the above cloud (ac) atmospheric radiance. This term is dependent upon the effective cloud vertical location. This dependence will be discussed in detail in later sections.

The cloud microphysical signature cannot be captured with the effective cloud emissivity alone for a given spectral channel or wavelength. It is the spectral variation of the effective cloud emissivity that holds the cloud microphysical information. To harness this information, the effective cloud emissivity is used to calculate effective absorption optical depth ratios; otherwise known as β-ratios (see Inoue 1987; Parol et al., 1991; Giraud et al., 1997; and Heidinger and Pavolonis, 2009). For a given pair of spectral emissivities ($\varepsilon(\lambda_1)$ and $\varepsilon(\lambda_2)$):

$$\beta_{obs} = \frac{\ln[1-\varepsilon(\lambda_1)]}{\ln[1-\varepsilon(\lambda_2)]} = \frac{\tau_{abs}(\lambda_1)}{\tau_{abs}(\lambda_2)} \quad \text{(Eq. 3)}$$

Notice that Equation 3 can simply be interpreted as the ratio of effective absorption optical depth (τ) at two different wavelengths. The word "effective" is used since the cloud emissivity depends upon the effective cloud temperature. The effective cloud temperature is most often different from the thermodynamic cloud top temperature since the cloud emission originates from a layer in the cloud. The depth of this layer depends upon the cloud transmission profile, which is generally unknown. One must also consider that the effects of cloud scattering are implicit in the cloud emissivity calculation since the actual observed radiance will be influenced by cloud scattering to some degree. In other words, no attempt is made to separate the effects and absorption and scattering. At wavelengths in the 10 to 13 μm range, the effects of cloud scattering for upwelling radiation are quite small and usually negligible. But at infrared wavelengths in the 8 – 10 μm range, the cloud reflectance can make a 1 – 3%

contribution to the top of atmosphere radiance (Turner, 2005). Thus, it is best to think of satellite-derived effective cloud emissivity as a radiometric parameter, which, in most cases, is proportional to the fraction of radiation incident on the cloud base that is absorbed by the cloud. See Cox (1976) for an in depth explanation of effective cloud emissivity.

An appealing quality of β_{obs}, is that it can be interpreted in terms of the single scatter properties, which can be computed for a given cloud composition and particle distribution. Following Van de Hulst (1980) and Parol et al. (1991), a spectral ratio of scaled extinction coefficients can be calculated from the single scatter properties (single scatter albedo, asymmetry parameter, and extinction cross section), as follows.

$$\beta_{theo} = \frac{[1.0 - \omega(\lambda_1)g(\lambda_1)]\sigma_{ext}(\lambda_1)}{[1.0 - \omega(\lambda_2)g(\lambda_2)]\sigma_{ext}(\lambda_2)} \quad \text{(Eq. 4)}$$

In Equation 4, β_{theo} is the spectral ratio of scaled extinction coefficients, ω is the single scatter albedo, g is the asymmetry parameter, and σ_{ext} is the extinction cross section. At wavelengths in the 8 – 15 μm range, where multiple scattering effects are small, β_{theo}, captures the essence of the cloudy radiative transfer such that,

$$\beta_{obs} \approx \beta_{theo} \quad \text{(Eq. 5)}$$

Equation 4, which was first shown to be accurate for observation in the 10 – 12 μm "window" by Parol et al. (1991), only depends upon the single scatter properties. It does not depend upon the observed radiances, cloud height, or cloud optical depth. By using β-ratios as opposed to brightness temperature differences, we are not only accounting for the non-cloud contribution to the radiances, we are also providing a means to tie the observations back to theoretical size distributions. This framework clearly has practical and theoretical advantages over traditional brightness temperature differences. Parol et al. (1991) first showed that Equation 5 is a good approximation. Since that time, faster computers and improvements in the efficiency and accuracy of clear sky radiative transfer modeling have allowed for more detailed exploration of the β data space and computation of β-ratios on a global scale. As such, Pavolonis (2010a) and Pavolonis (2010b) showed that β-ratios offer improved sensitivity to the presence of volcanic ash relative to brightness temperature differences for the same channel pair.

3.4.1.2 Cloud Composition Differences in β-Space

Three channel pairs are used in the volcanic ash detection algorithm *(two channel pairs for VIIRS-VAA)*, the 8.5, 11 μm pair (ABI Channels 11 and 14, VIIRS Channels 14 and 15), the 11, 12 μm pair (ABI Channels 14 and 15, VIIRS Channels 15 and 16), and the 7.4, 11 μm pair (ABI Channels 10 and 14, not applicable for VIIRS). From these channel pairs, β-ratios were constructed such that the 11 μm channel is always placed in the denominator of Equations 3 and 4. Hereafter, these β's are referred to as β(8.5/11μm) and β(12/11μm). The single scatter property relationship (Equation 4) can be used to

establish a theoretical relationship for these β's as a function of cloud composition and cloud particle size. Figure 3 shows the relationship between β(8.5/11μm) and β(12/11μm) as given by the single scatter properties (see Equation 4) for various cloud compositions with a varying effective particle radius. With the exception of ice, all single scatter properties were calculated using Mie theory. The ice single scatter properties were taken from the Yang et al. (2005) database for various ice crystal habits. From this figure, one can see that separating meteorological cloud from ash or dust clouds can be effectively accomplished using a tri-spectral (8.5, 11, 12 μm) technique. Differentiating between ash and dust, however, requires additional information. Unlike brightness temperature differences, these β relationships are only a function of the cloud microphysical properties.

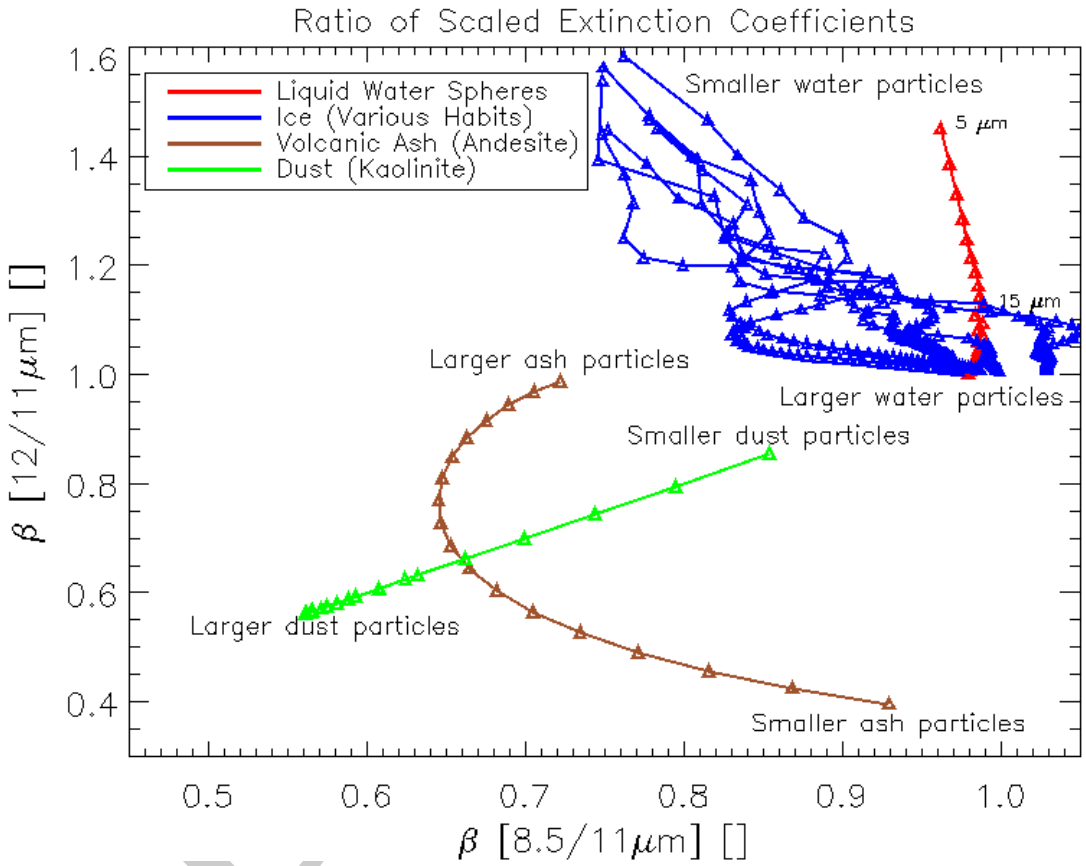

Figure 3: The 12/11 μm scaled extinction ratio (β(12/11μm)) is shown as a function of the 8.5/11 μm scaled extinction ratio (β(8.5/11μm)) for liquid water spheres (red), various ice habits (blue), andesite spheres (brown), and kaolinite spheres (green). A range of particle sizes is shown for each composition. For liquid water and ice, the effective particle radius was varied from 5 to 54 μm. The andesite and kaolinite effective particle radius was varied from 1 to 12 μm. The large and small particle ends of each curve are labeled. These β-ratios were derived from the single scatter properties.

3.4.2 **Mathematical Description – Volcanic Ash Detection**

3.4.2.1 Converting the Measured Radiances to Emissivities and β-Ratios

3.4.2.1.1 Single Layer Tropopause Assumption

The first formulation assumes a constant effective cloud level consistent with the thermodynamic tropopause given by Numerical Weather Prediction (NWP) data (see the AIADD Document for more information). Equations 6a – 6g specifically show how this assumption is applied to Equations 2 and 3 for the channel pairs used in the volcanic ash algorithm. In these equations, $\varepsilon_{stropo}(\lambda)$ is the spectral cloud emissivity computed using the single layer tropopause assumption, and $\beta_{stropo}(\lambda_1/\lambda_2)$ represents the β calculated from this type of cloud emissivity. T_{tropo} is the temperature of the tropopause. $R_{tropo}(\lambda)$ and $t_{tropo}(\lambda)$ are the clear sky atmospheric radiance and transmittance, vertically integrated from the tropopause to the top of the atmosphere, respectively (the calculation of the clear sky radiance and transmittance are described in detail in the AIADD Document). All other terms were defined previously. This formulation is primarily useful for detecting optically thin ash clouds.

$$\varepsilon_{stropo}(7.4\mu m) = \frac{R_{obs}(7.4\mu m) - R_{clr}(7.4\mu m)}{[B(7.4\mu m, T_{tropo})t_{tropo}(7.4\mu m) + R_{tropo}(7.4\mu m)] - R_{clr}(7.4\mu m)} \quad \text{(Eq. 6a) } \textit{(ABI-VAA only)}$$

$$\varepsilon_{stropo}(8.5\mu m) = \frac{R_{obs}(8.5\mu m) - R_{clr}(8.5\mu m)}{[B(8.5\mu m, T_{tropo})t_{tropo}(8.5\mu m) + R_{tropo}(8.5\mu m)] - R_{clr}(8.5\mu m)} \quad \text{(Eq. 6b)}$$

$$\varepsilon_{stropo}(11\mu m) = \frac{R_{obs}(11\mu m) - R_{clr}(11\mu m)}{[B(11\mu m, T_{tropo})t_{tropo}(11\mu m) + R_{tropo}(11\mu m)] - R_{clr}(11\mu m)} \quad \text{(Eq. 6c)}$$

$$\varepsilon_{stropo}(12\mu m) = \frac{R_{obs}(12\mu m) - R_{clr}(12\mu m)}{[B(12\mu m, T_{tropo})t_{tropo}(12\mu m) + R_{tropo}(12\mu m)] - R_{clr}(12\mu m)} \quad \text{(Eq. 6d)}$$

$$\beta_{stropo}(8.5/11\mu m) = \frac{\ln[1-\varepsilon_{tropo}(8.5\mu m)]}{\ln[1-\varepsilon_{tropo}(11\mu m)]} \quad \text{(Eq. 6e)}$$

$$\beta_{stropo}(12/11\mu m) = \frac{\ln[1-\varepsilon_{tropo}(12\mu m)]}{\ln[1-\varepsilon_{tropo}(11\mu m)]} \quad \text{(Eq. 6f)}$$

$$\beta_{stropo}(7.4/11\mu m) = \frac{\ln[1-\varepsilon_{tropo}(7.4\mu m)]}{\ln[1-\varepsilon_{tropo}(11\mu m)]} \quad \text{(Eq. 6g) } \textit{(ABI-VAA only)}$$

3.4.2.1.2 Multilayered Tropopause Assumption

Similar to the first formulation, the second cloud vertical level formulation assumes that the cloud vertical level is the tropopause level (given by NWP). Unlike the first formulation, this one includes an additional twist. In this formulation, the clear sky top-of-atmosphere radiance is replaced by the top-of-atmosphere radiance originating from a black (e.g. emissivity = 1.0 at all wavelengths) elevated surface. The elevated black surface is used to roughly approximate a blackbody cloud in the lower troposphere. The black surface is placed at height equal to the surface pressure minus 200 mb. The ability to detect multilayered clouds with infrared measurements is predicated on the lower cloud layer being colder than the surface and the upper cloud layer being colder than the lower cloud layer (Pavolonis and Heidinger, 2004). The surface pressure minus 200 mb was chosen as a compromise of these two factors. The pressure level (P_{black}) of this black surface is given by Equation 7. In Equation 7, $P_{surface}$ is the pressure of the lowest level in the NWP atmospheric pressure profile. The purpose of this formulation is to help detect volcanic ash clouds that overlap lower meteorological cloud layers. Equations 8a – 8g specifically show how this assumption is applied to Equations 2 and 3 for the channel pairs used in the volcanic ash algorithm. In these equations, $\varepsilon_{mtropo}(\lambda)$ is the spectral cloud emissivity computed using this formulation, and β_{mtropo} (λ_1/λ_2) represents the β calculated from this type of cloud emissivity. T_{black} is the temperature at the pressure level, P_{black}. $R_{black}(\lambda)$ and $t_{black}(\lambda)$ are the clear sky atmospheric radiance and transmittance, vertically integrated from the level where the atmospheric pressure is equal to P_{black} to the top of the atmosphere, respectively. The $R_{black}(\lambda)$ and $t_{black}(\lambda)$ terms are simply pulled from pre-calculated profiles of clear sky atmospheric radiance and transmittance using the profile level returned by a standard generic binary search routine when the atmospheric pressure profile is searched for P_{black} (e.g. no interpolation is performed). The derivation of the pre-calculated clear sky atmospheric radiance and transmittance profiles is described in detail in the AIADD Document. All other terms in Equation 8a – 8g were previously defined.

$$P_{black} = P_{surface} - 200mbar \quad \text{(Eq. 7)}$$

$$\varepsilon_{mtropo}(7.4\mu m) = \frac{R_{obs}(7.4\mu m) - [B(7.4\mu m, T_{black})t_{black}(7.4\mu m) + R_{black}(7.4\mu m)]}{[B(7.4\mu m, T_{tropo})t_{tropo}(7.4\mu m) + R_{tropo}(7.4\mu m)] - [B(7.4\mu m, T_{black})t_{black}(7.4\mu m) + R_{black}(7.4\mu m)]}$$

(Eq. 8a) *(ABI-VAA only)*

$$\varepsilon_{mtropo}(8.5\mu m) = \frac{R_{obs}(8.5\mu m) - [B(8.5\mu m, T_{black})t_{black}(8.5\mu m) + R_{black}(8.5\mu m)]}{[B(8.5\mu m, T_{tropo})t_{tropo}(8.5\mu m) + R_{tropo}(8.5\mu m)] - [B(8.5\mu m, T_{black})t_{black}(8.5\mu m) + R_{black}(8.5\mu m)]}$$

(Eq. 8b)

$$\varepsilon_{mtropo}(11\mu m) = \frac{R_{obs}(11\mu m) - [B(11\mu m, T_{black})t_{black}(11\mu m) + R_{black}(11\mu m)]}{[B(11\mu m, T_{tropo})t_{tropo}(11\mu m) + R_{tropo}(11\mu m)] - [B(11\mu m, T_{black})t_{black}(11\mu m) + R_{black}(11\mu m)]}$$

(Eq. 8c)

$$\varepsilon_{mtropo}(12\mu m) = \frac{R_{obs}(12\mu m) - [B(12\mu m, T_{black})t_{black}(12\mu m) + R_{black}(12\mu m)]}{[B(12\mu m, T_{tropo})t_{tropo}(12\mu m) + R_{tropo}(12\mu m)] - [B(12\mu m, T_{black})t_{black}(12\mu m) + R_{black}(12\mu m)]}$$

(Eq. 8d)

$$\beta_{mtropo}(8.5/11\mu m) = \frac{\ln[1-\varepsilon_{tropo}(8.5\mu m)]}{\ln[1-\varepsilon_{tropo}(11\mu m)]}$$ (Eq. 8e)

$$\beta_{mtropo}(12/11\mu m) = \frac{\ln[1-\varepsilon_{tropo}(12\mu m)]}{\ln[1-\varepsilon_{tropo}(11\mu m)]}$$ (Eq. 8f)

$$\beta_{mtropo}(7.4/11\mu m) = \frac{\ln[1-\varepsilon_{tropo}(7.4\mu m)]}{\ln[1-\varepsilon_{tropo}(11\mu m)]}$$ (Eq. 8g) *(ABI-VAA only)*

3.4.2.1.3 Single Layer Opaque Cloud Assumption

This formulation uses the opaque cloud assumption discussed in Pavolonis (2010a). In this case, the effective cloud vertical level is taken to be the level where either the 11 or 12 μm cloud emissivity is equal to 0.98. The 7.4 *(ABI-VAA only)* and 8.5 μm channels are not used in this formulation. This formulation is used to help separate ice clouds from volcanic ash, as described in a later section. The process for implementing this formulation is as follows.

1. For a given channel (11 and 12 μm), Equation 2 is rearranged to solve for the black cloud radiance term, $R_{cld}(\lambda)$, that is needed to yield a cloud emissivity of 0.98. Equation 9 shows this rearrangement. In this assumption, the cloud emissivity, $\varepsilon(\lambda)$, in Equation 9 is set to 0.98.

$$R_{cld}(\lambda) = \frac{R_{obs}(\lambda) + R_{clr}(\lambda)[\varepsilon(\lambda) - 1]}{\varepsilon(\lambda)}$$ (Eq. 9) where

$$R_{cld}(\lambda) = B(\lambda, T_{eff})t_{ac}(\lambda) + R_{ac}(\lambda)$$ (Eq. 10)

2. For a given channel, the $R_{cld}(\lambda)$ calculated in Step 1 is compared to a pre-calculated vertical profile of $R_{cld}(\lambda)$ for the same channel (see the AIADD Document). The profile of $R_{cld}(\lambda)$ is used to determine the weight and anchor points needed to linearly interpolate the profile of $R_{cld}(\lambda)$ to the value calculated

using Equation 9 with the assumption that $\varepsilon(\lambda) = 0.98$. Equation 11 shows how the interpolation weight, $W(\lambda,0.98)$, is determined.

$$W(\lambda,0.98) = \frac{R_{cld}(\lambda,0.98) - R_{cld}(\lambda,Z_1)}{R_{cld}(\lambda,Z_2) - R_{cld}(\lambda,Z_1)} \quad \text{(Eq. 11)}$$

In Equation 11, $R_{cld}(\lambda, 0.98)$ is the value calculated using Equation 9 with the assumption that $\varepsilon(\lambda) = 0.98$. $R_{cld}(\lambda,Z_1)$ and $R_{cld}(\lambda,Z_2)$ are the black cloud radiances within the vertical profile that bound $R_{cld}(\lambda,0.98)$, with $R_{cld}(\lambda,Z_1)$ being the black cloud radiance at the highest (e.g. furthest from the ground) bounding level (Z_1). Z_1 and Z_2 are the vertical array indices corresponding to the interpolation anchor points.

3. Steps 1 and 2 are performed for the 11 and 12 μm channels. The interpolation weights and anchor points associated with each channel are used to determine which $R_{cld}(\lambda,0.98)$ occurs at the highest (e.g. furthest from the ground) vertical level.

4. Once it is determined for which channel $R_{cld}(\lambda,0.98)$ occurs at the highest vertical level, the interpolation weight and anchor points for that channel are used to interpolate the $R_{cld}(\lambda)$ of the other two channels to that same level. The highest level is chosen to prevent the cloud emissivity in any of the channels from becoming too large (e.g. > 1.0). Thus, the cloud emissivity is fixed at 0.98 for the channel where an emissivity of 0.98 occurs at the highest vertical level. This channel is referred to as the reference channel. The interpolation of $R_{cld}(\lambda)$ for the non-reference channels is performed according to Equation 12. Note that by interpolating $R_{cld}(\lambda)$, for the non-reference channels, to the level where the $R_{cld}(\lambda)$ of the reference channel gives an emissivity equal to 0.98, allows the emissivty of the non-reference channels to deviate from 0.98. Recall that cloud microphysical information is related to the spectral variation of cloud emissivity. In Equation 12, $R_{cld\_int}(\lambda)$ is the upwelling black cloud radiance interpolated using the reference weight [$W(\lambda_{ref},0.98)$] and reference anchor points [$R_{cld}(\lambda_{ref},Zref_1)$ and $R_{cld}(\lambda_{ref},Zref_2)$] that give a cloud emissivity of 0.98 at the reference channel. $Zref_1$ and $Zref_2$ are the vertical array indices of the reference interpolation anchor points.

$$R_{cld\_int}(\lambda) = R_{cld}(\lambda,Zref_1) + W(\lambda_{ref},0.98)[R_{cld}(\lambda,Zref_2) - R_{cld}(\lambda,Zref_1)] \quad \text{(Eq. 12)}$$

5. Finally, the 11 and 12 μm channel cloud emissivities are computed using Equations 13a – 13b. $\beta(12/11\mu m)$ is also computed using Equation 13c. In these equations, $\varepsilon_{sopaque}(\lambda)$ is the spectral cloud emissivity computed using the single layer opaque cloud assumption, and $\beta_{sopaque}(\lambda_1/\lambda_2)$ represents the β calculated from this type of cloud emissivity. If this formulation is implemented correctly, $\varepsilon_{sopaque}(\lambda)$ at the reference channel should be equal to 0.98.

$$\varepsilon_{sopaque}(11\mu m) = \frac{R_{obs}(11\mu m) - R_{clr}(11\mu m)}{R_{cld\_interp}(11\mu m) - R_{clr}(11\mu m)} \quad \text{(Eq. 13a)}$$

$$\varepsilon_{sopaque}(12\mu m) = \frac{R_{obs}(12\mu m) - R_{clr}(12\mu m)}{R_{cld\_interp}(12\mu m) - R_{clr}(12\mu m)} \quad \text{(Eq. 13b)}$$

$$\beta_{sopaque}(12/11\mu m) = \frac{\ln[1 - \varepsilon_{sopaque}(12\mu m)]}{\ln[1 - \varepsilon_{sopaque}(11\mu m)]} \quad \text{(Eq. 13c)}$$

3.4.2.1.4 Multilayered Opaque Cloud Assumption

This assumption is implemented in exactly the same manner as the "Single Layer Opaque Cloud Assumption" except the top-of-atmosphere clear sky radiance is replaced by the top-of-atmosphere radiance originating from a black elevated surface. Just as in the "Multilayered Tropopause Assumption," the black surface is placed at the 0.8 sigma level in a terrain following coordinate system. The black elevated surface is explained in detail in Section 3.4.2.1.2. As explained in a later section, the "Multilayered Opaque Cloud Assumption" is used to help detect volcanic ash that overlaps lower level meteorological clouds. In this formulation, the 11 and 12 μm channel cloud emissivities are computed using Equations 14a – 14b (the 7.4 and 8.5 μm channels are not used in this formulation). β(12/11μm) is also computed using Equation 14c In these equations, $\varepsilon_{mopaque}(\lambda)$ is the spectral cloud emissivity computed using the multilayered opaque cloud assumption, and $\beta_{mopaque}(\lambda_1/\lambda_2)$ represents the β calculated from this type of cloud emissivity.

$$\varepsilon_{mopaque}(11\mu m) = \frac{R_{obs}(11\mu m) - [B(11\mu m, T_{black})t_{black}(11\mu m) + R_{black}(11\mu m)]}{R_{cld\_interp}(11\mu m) - [B(11\mu m, T_{black})t_{black}(11\mu m) + R_{black}(11\mu m)]} \quad \text{(Eq. 14a)}$$

$$\varepsilon_{mopaque}(12\mu m) = \frac{R_{obs}(12\mu m) - [B(12\mu m, T_{black})t_{black}(12\mu m) + R_{black}(12\mu m)]}{R_{cld\_interp}(12\mu m) - [B(12\mu m, T_{black})t_{black}(12\mu m) + R_{black}(12\mu m)]} \quad \text{(Eq. 14b)}$$

$$\beta_{mopaque}(12/11\mu m) = \frac{\ln[1 - \varepsilon_{mopaque}(12\mu m)]}{\ln[1 - \varepsilon_{mopaque}(11\mu m)]} \quad \text{(Eq. 14c)}$$

3.4.2.2 Median Spatial Filter

The emissivity described in Section 3.4.2.1 can, at times, be noisy, especially near cloud edges, in areas of broken clouds, and for very small cloud optical depths. In order to minimize the occurrence of "salt and pepper" noise, a standard 3 x 3 median filter is applied to the $\varepsilon_{stropo}(11\mu m)$. The median filter simply replaces the value at each pixel

with the median value of a 3 x 3 pixel array centered on that pixel. The generic median filter procedure is described in the AIADD Document.

3.4.2.3 Identifying a Pixel's Local Radiative Center

In regions where the radiative signal of a cloud is small, like cloud edges, the various β-ratios are difficult to interpret since the cloud fraction, which is assumed to be 1.0, may be less than 1.0, or very small cloud optical depths may produce a signal that cannot be differentiated from noise. With the spectral information limited, a spatial metric is needed to make a spatially and physically consistent cloud type determination for these types of pixels. To address this problem, the gradient filter procedure, which is described in detail in the AIADD Document, is used to determine the Local Radiative Center (LRC) of each pixel valid pixel. A pixel is valid if it has a valid Earth latitude and longitude and has valid spectral data (based on the L1b calibration flags). The $\varepsilon_{stropo}(11\mu m)$ parameter described in Section 3.4.2.1 is used to compute the LRC. The gradient filter inputs (which are described in detail in the AIADD Document) for this application are listed in Table 5.

Gradient Variable	Minimum Valid Value of Gradient Variable	Maximum Valid Value of Gradient Variable	Gradient Stop Value	Apply Gradient Filter To
$\varepsilon_{Stropo}(11\mu m)$	0.0	1.0	0.7	All pixels with a valid Earth lat/lon and valid spectral data for ABI channels 10, 11, 14, and 15 (VIIRS channels 11, 14, and 15).

Table 5: Inputs used in calculation of Local Radiative Center (LRC). The gradient filter function used in the calculation is described in the AIADD document.

The gradient filter allows one to consult the spectral information at an interior pixel within the same cloud in order to avoid using the spectral information offered by pixels with a very weak cloud radiative signal or sub-pixel cloudiness associated with cloud edges. Overall, this use of spatial information allows for a more spatially and physically consistent product. This concept is also explained in Pavolonis (2010b).

3.4.2.4 Volcanic Ash Detection Rules

Volcanic ash detection is performed by applying rules to the radiative parameters derived in the previous sections. These rules are described in the following four subsections. Before applying volcanic ash detection rules, the input data are checked for validity. If a pixel is an Earth pixel (e.g.—not a space pixel) and the required spectral channels are not identified as bad by the L1b calibration quality flag, the Ash Detection QF flags, Invalid_Data_Qf and Overall_Qf data are set to high quality, respectively. Otherwise they are set to low quality the pixel is cycled. Additionally the Ash Detection QF

Satzen_Qf Flag is set to low quality for satellite zenith angles greater than 80 degrees otherwise it is high quality. After all the filters in the following three subsections have been applied the final ash confidence is stored in the Ash Detection QF Flag Ash_Single_Layer_Conf_Qf. All of the ash detection product quality flags are defined in Table 20.

Figure 4 shows a high-level flow chart of the ash detection algorithm. The basic flow of the algorithm checks for valid data, assigns an initial ash confidence, runs through ash confidence adjustment filters, runs through additional ash quality control filters, and outputs a final ash confidence (single layer and multiple layer confidences). The retrieval algorithm uses the ash confidence information to determine when to perform retrieval and what assumptions (single or multilayered) should be made within the retrieval.

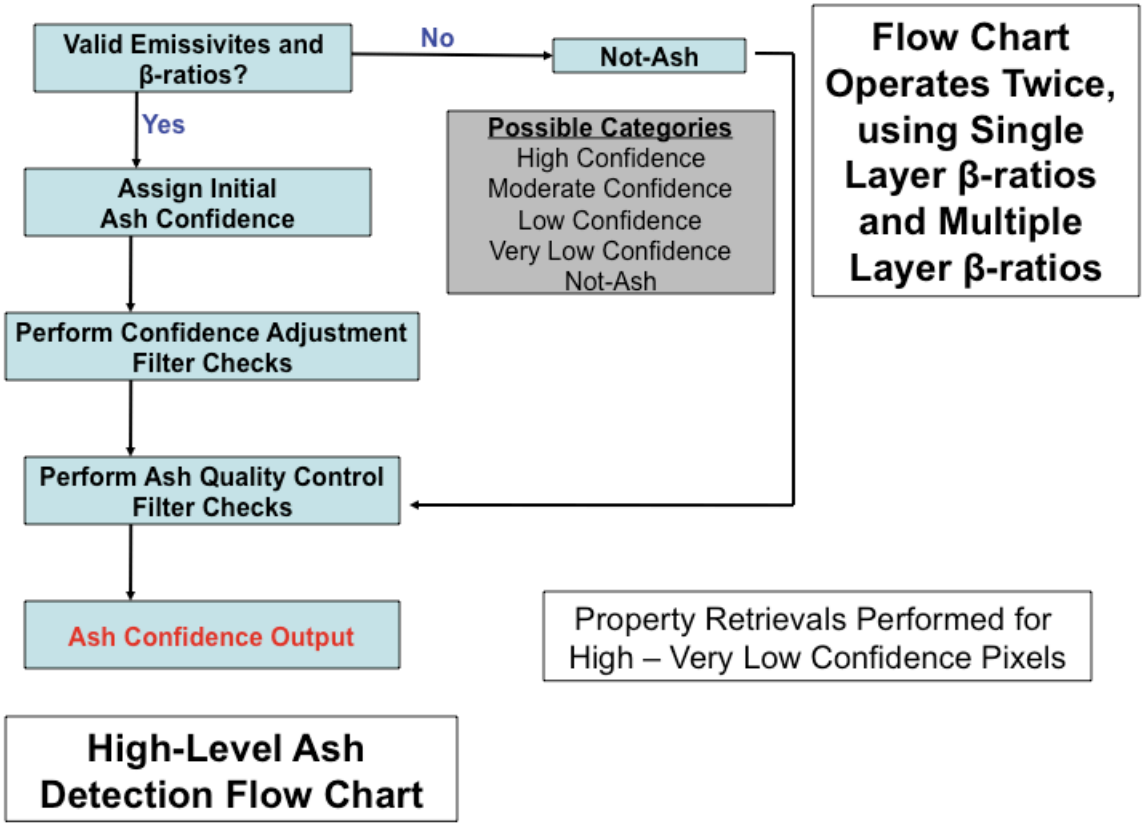

Figure 4: High-level flow chart of ash detection algorithm. The column of blue boxes on the left side of the flowchart represents the following three subsections in the text.

Table 6 describes three ash confidence terms used within the following four subsections. These terms are defined here to enhance text clarity.

Term	Description
'Pixel Confidence'	Ash confidence at the pixel

'LRC Confidence'	Ash confidence at the pixel's local radiative center (LRC)
'Summed Confidence'	Summed ash confidence of Pixel Confidence and LRC Confidence

Table 6: Ash confidence terminology used throughout the ash detection subsections.

3.4.2.4.1 Initial Ash Confidence Using β-ratios

1. An initial ash confidence is assigned for each pixel. Only pixels with $\varepsilon_{stropo}(11\mu m) \geq 0.02$ (see Equation 6b), $\varepsilon_{stropo}(8.5\mu m) \geq 0.02$ (see Equation 6a), $\beta_{stropo}(12/11\ \mu m) > 0.0$ (see Equation 6f), $\beta_{stropo}(12/11\ \mu m) < 1.00$ (see Equation 6f), $\beta_{stropo,lrc}(12/11\ \mu m) > 0.0$, $\beta_{stropo,lrc}(12/11\ \mu m) < 1.00$, $\beta_{stropo}(8.5/11\ \mu m) > 0.0$, $\beta_{stropo}(8.5/11\ \mu m) < 10.0$ (see Equation 6e), $\beta_{stropo,lrc}(8.5/11\ \mu m) > 0.0$, and $\beta_{stropo,lrc}(8.5/11\ \mu m) < 10.0$, are considered candidates for containing volcanic ash. This rule ensures that the ash/no ash decision is based on a minimum radiative signal and within a wide acceptable range of β-ratios. A pixel not meeting the criterion above is assigned a 'Summed Confidence' of "not-ash" (See Table 8 for description of ash confidence values).

2. The $\beta_{stropo}(8.5/11\mu m)$ and $\beta_{stropo}(12/11\mu m)$ (see Equations 6e and 6f) at each pixel, that meets the criterion outlined in the first rule, is used to assign the 'Pixel Confidence'. The 'Pixel Confidence' can have the following values: "high" confidence, "moderate" confidence, or "not-ash." Confidence is measured by how closely $\beta_{stropo}(8.5/11\mu m)$ and $\beta_{stropo}(12/11\mu m)$ match the theoretical ash cloud values (given by Equation 4) for the same channel combinations. These theoretical values are shown in Figure 3. Figure 5 shows a schematic how ash confidence flags are assigned for a combination of $\beta_{stropo}(8.5/11\mu m)$ (or $\beta_{mtropo}(8.5/11\mu m)$) and $\beta_{stropo}(12/11\mu m)$ (or $\beta_{mtropo}(8.5/11\mu m)$). Table 7 describes the lines separating ash confidence zones in Figure 5.

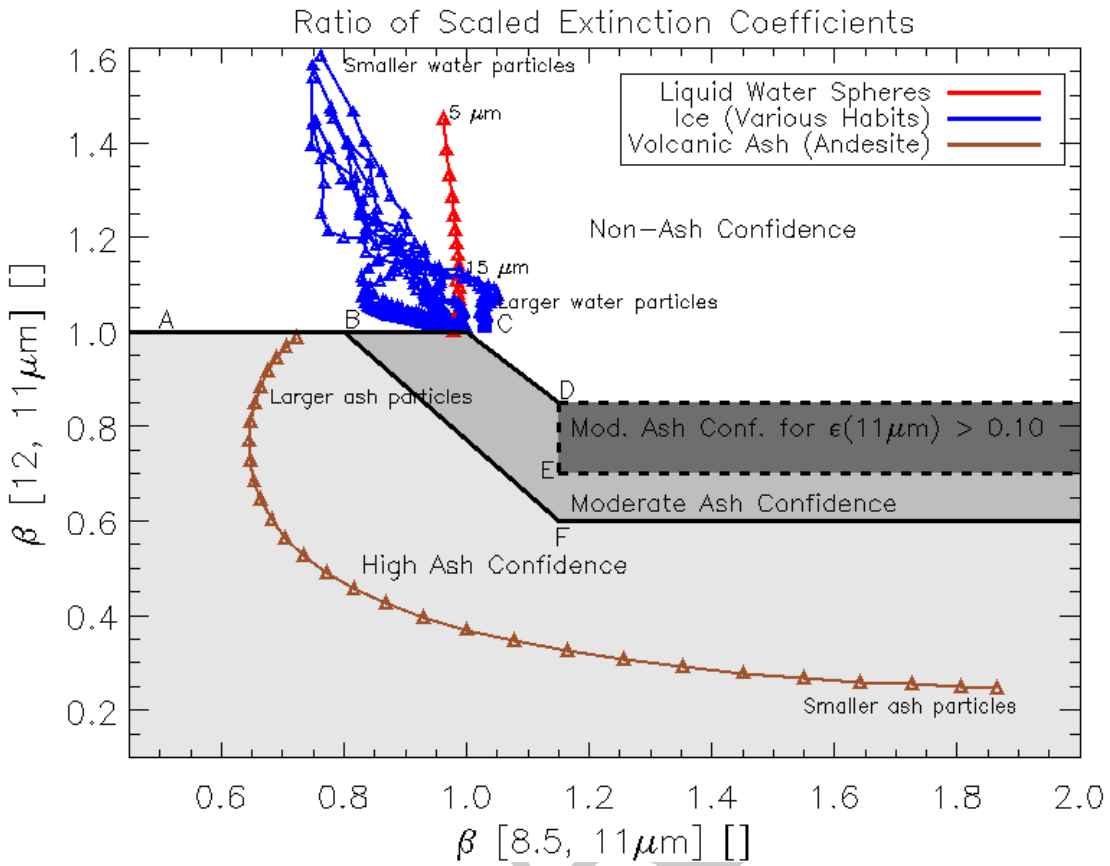

Figure 5: The 2-d β_{stropo}(8.5/11μm) (or β_{mtropo}(8.5/11μm)) and β_{stropo}(12/11μm) (or β_{mtropo}(12/11μm)) curves for ash, water cloud, and ice cloud. The ash confidence zones are shaded, light gray for "high" confidence, medium gray for "moderate" ash confidence, dark gray for "moderate" ash confidence for pixels with ε_{stropo}(11μm) > 0.10 (or ε_{mtropo}(11μm) > 0.10), and white for "not-ash". These ash confidence zones are used in Rule 2 and Rule 3 of section 3.4.2.4.1. The slopes, intercepts, and thresholds for the lines making the ash confidence zones are detailed in Table 7.

Line Segment	Begin β (8.5/11μm) Threshold	End β (8.5/11μm) Threshold	Begin β (12/11μm) Threshold	End β (12/11μm) Threshold	Slope	Intercept
A → B	0.00	0.80	1.00	1.00	0.000	1.000
B → C	0.80	1.00	1.00	1.00	0.000	1.000
C → D	1.00	1.15	1.00	0.85	-1.000	2.000
B → F	0.80	1.15	1.00	0.60	-1.140	1.912
D → ∞	1.15	10.0	0.85	0.85	0.000	0.850
E → ∞	1.15	10.0	0.70	0.70	0.000	0.700
F → ∞	1.15	10.0	0.60	0.60	0.000	0.600

Table 7: Description of β thresholds, slopes, and intercepts for lines constructing ash confidence zones in Figure 5.

3. Regarding boundaries of ash confidence zones, the following rules apply. Any pixel on any border of the moderate confidence zone belongs to moderate confidence (e.g.-the moderate confidence box and its boundaries are inclusive for moderate confidence). High confidence pixels must lie in its respective zone, not on the lines. So if a pixel lies on a boundary between high confidence and a lower confidence zone, the pixel goes to the lower confidence zone. One special case exists, the left edge of the expanded moderate confidence box for pixels with $\varepsilon_{stropo}(11\mu m) > 0.10$ is not inclusive, the pixel must have $\beta_{stropo}(8.5/11\mu m) >$ the threshold indicated in Table 7. Additionally, if a pixel falls into the expanded moderate confidence box, but has $\varepsilon_{stropo}(11\mu m) <= 0.10$, the pixel is assigned non-ash confidence.

4. Rule 2 is repeated using $\beta_{stropo,lrc}(8.5/11\mu m)$ and $\beta_{stropo,lrc}(12/11\mu m)$. The result of this test is known as the 'LRC Confidence'.

5. The 'Pixel Confidence' and 'LRC Confidence' are summed together. This sum is referred to as the 'Summed Confidence'. Any 'Summed Confidence' greater than "low" is set to "not-ash." Table 8 describes the possible ash confidence values. Notice 0, 1, 2, and values ≥ 4 are the only possibilities for the 'Summed Confidence'. The value of 3 ("very low" confidence) is reserved for use in ash filters described in sections 3.4.2.4.2 and 3.4.2.4.3 and the value of two cannot be assigned using Rule 2 (see Figure 5).

Ash Confidence	Integer Value	Description
High	0	High confidence pixel contains ash
Moderate	1	Moderate confidence pixel contains ash
Low	2	Low confidence pixel contains ash
Very Low	3	Very low confidence pixel contains ash
Not-Ash	4	High confidence that pixel does not contain ash

Table 8: The ash confidence range of possible values. The "high, moderate, and not-ash" categories are used in assigning 'Pixel Confidence' and 'LRC Confidence' (Rules 2 and 3, respectively). The "low" confidence category occurs in the 'Summed Confidence' only, via the summations of the 'Pixel Confidence' and 'LRC Confidence'. The "very low" confidence category can only result from the ash confidence adjustment filters described in the next section.

3.4.2.4.2 Ash Confidence Adjustment Filters

After the rules in section 3.4.2.4.1 are completed, a series of ash confidence adjustment filters are applied to the pixels meeting the requirements of Rule 1 in Section 3.4.2.4.1. The ash confidence adjustment filters are described below.

1. The first filter checks for the spectral signatures of sulfur dioxide (SO_2) in combination with a sufficiently negative (11μm – 12μm) brightness temperature

difference (BTD1112), as this is a strong indicator of an SO_2 cloud that vertically overlaps an ash cloud.

Filter implementation: The results of this filter are stored in two Ash Detection PQI flags and are used in subsequent tests within this section. Weak_Btd_Strong_SO_2 signal is when $\varepsilon_{tropo}(8.5\mu m) > \varepsilon_{tropo}(11\mu m)$, $\varepsilon_{tropo}(7.4\mu m) > \varepsilon_{tropo}(8.5\mu m)$, and BTD1112 $\leq$ 0.0. If Weak_Btd_Strong_SO_2 is not present, then the Strong_Btd_Weak_SO_2 signal is tested for and true when $\varepsilon_{tropo}(8.5\mu m) > \varepsilon_{tropo}(11\mu m)$ and BTD1112 $\leq$ -0.75 K. *For VIIRS-VAA Weak_Btd_Strong_SO2 will always be set to false due to lack of 7.4 µm channel from VIIRS.*

2. The second ash confidence adjustment filter is used to increase the 'Summed Confidence' of "low confidence/non-ash" when there is a strong BTD1112 signal, weak SO_2 signature present. This is designed to capture volcanic clouds with a SO_2 signal that may otherwise obscure ash at 8.5 µm, where SO_2 absorbs.

   Filter implementation: If the Strong_Btd_Weak_SO_2_Single_Layer_Flag is true and 'Summed Confidence' is "low" confidence or ['Pixel Confidence' is "high" or "moderate" confidence and the 'LRC Confidence' is "not-ash" confidence]; the 'Summed Confidence' is set to "moderate" ash confidence.

3. The third confidence adjustment filter is used to increase the 'Summed Confidence' of "low confidence/non-ash" classified pixels when there is a weak BTD1112 signal, strong SO_2 signature present. This is designed to capture volcanic clouds with a SO_2 signal that may otherwise obscure ash.

   Filter implementation: If the Weak_Btd_Strong_SO_2_Single_Layer_Flag is true and the 'Summed Confidence' is "low" confidence or ['Pixel Confidence' is "high" or "moderate" confidence and the 'LRC confidence' is "not-ash" confidence]; the 'Summed Confidence' is set to "moderate" ash confidence.

4. The fourth ash confidence adjustment filter is used to identify any remaining "not-ash" pixels (after Filters 2 and 3 of this section have been applied) that had both a SO_2 signal and sufficiently small BTD1112.

   Filter implementation: If the 'Summed Confidence' is "not-ash" and either the Strong_Btd_Weak_SO_2_Single_Layer_Flag or Weak_Btd_Strong_SO_2_Single_Layer_Flag is true; the 'Summed Confidence' is set to "very low" confidence.

5. The fifth confidence adjustment filter is used to increase the 'Summed Confidence' of "not-ash" classified pixels when there is at least a weak BTD1112 signal, 'Pixel Confidence' was "high" or "moderate" and the 'LRC Confidence' was "not-ash." This test is intended to capture very thin ash that might be spatially adjacent to optically thicker meteorological clouds, and hence was not

previously detected as ash (e.g. the LRC is located in meteorological cloud, not ash).

Filter implementation: This filter is implemented as follows. If the 'Pixel Confidence' is "high" or "moderate" confidence and 'LRC Confidence' is "not-ash" and BTD1112 < 1.00 K then the 'Summed Confidence' is set to "low confidence."

6. The sixth ash confidence adjustment filter is used to increase the 'Summed Confidence' of "low" and "very low" confidence classifications that have a sufficiently small BTD1112 and either 'Pixel Confidence' or 'LRC Confidence' of "high" or "moderate" confidence. This test is intended to make sure a strong BTD1112 signal in conjunction with at least one test ('Pixel Confidence' or 'LRC Confidence') suggesting "high" or "moderate" confidence is included in the "moderate" confidence category.

   Filter implementation: If the 'Summed Confidence' is equal to "low" or "very low" confidence and BTD1112 < -0.75 K and either 'Pixel Confidence' or 'LRC Confidence' is equal to "high" or "moderate" confidence then the 'Summed Confidence' is set to "moderate" confidence.

3.4.2.4.3 Ash Quality Control Filters

The following ash quality control filters operate on all valid Earth pixels, including those that do not meet the emissivity and β thresholds described in Rule 1 of section 3.4.2.4.1.

1. The first filter described in this section reclassifies "not-ash" 'Summed Confidence' pixels to the "very low" ash confidence category if they have a sufficiently negative BTD1112, which can be a signal of volcanic ash (e.g. Prata, 1989).

   Filter implementation: If a pixel has a 'Summed Confidence' equal to "not-ash" and the BTD1112 is less than a threshold; the 'Summed Confidence' is set to "very low." The BTD1112 threshold used in this filter is dynamic, and is a function of the split window (11 μm - 12 μm) surface emissivity difference (SWSED) and is described in Table 9 below.

Split-Window Surface Emissivity Difference (SWSED) (11 μm – 12 μm)	**BTD1112 Threshold (K)**
$-1.0x10^{-3} < SWSED < -1.0x10^{-6}$	-0.75
$SWSED <= -1.0x10^{-3}$	-1.00
All other values of SWSED	-0.50

Table 9: BTD1112 thresholds used within Filter 1 of section 3.4.2.4.3 depending upon the split-window surface emissivity difference (11 μm – 12 μm).

2. The second filter is used to reclassify pixels with a 'Summed Confidence' equal to "high" to "moderate" if the pixel $\varepsilon_{tropo}(11\mu m)$ is sufficiently small.

Filter implementation: If a pixel has 'Summed Confidence' equal to "high" and a $\varepsilon_{tropo}(11\mu m) < 0.05$ set 'Summed Confidence' to "moderate."

3. The third filter is used to eliminate optically thick ice clouds.

   Filter implementation: If a pixel has $\varepsilon_{tropo}(11\mu m) > 0.50$, $\beta_{tropo}(7.3\mu m/11\ \mu m) < 1.00$, $\beta_{tropo}(7.3\mu m/11\ \mu m) > 0.00$, and $\beta_{sopaque}(12/11\mu m) \geq 1.00$ set 'Summed Confidence' to "not-ash." *This filter will always be set to false for VIIRS-VAA since the 7.3 μm is not available from VIIRS.*

4. The fourth filter eliminates ash pixels with large satellite zenith angles (θ_{sat}) if $\beta(12/11\ \mu m)$ is too large. As θ_{sat} increases the spectral separation between meteorological cloud (water and ice) and ash clouds becomes smaller (Pavolonis 2010b). To account for this, pixels with sufficiently large θ_{sat} are required to have increasingly small $\beta(12/11\ \mu m)$.

   Filter implementation: If a pixel has a $\theta_{sat} < 75$ degrees this filter is not applied. If a pixel has a $\theta_{sat} > 80$ degrees the 'Summed Confidence' is automatically set to "not-ash" confidence. If a pixel has a $\theta_{sat} \geq 75$ degrees and ≤ 80 degrees the 'Summed Confidence' is set to "not-ash" confidence if $\beta_{stropo}(12/11\ \mu m)$ is larger than a threshold. The $\beta_{stropo}(12/11\ \mu m)$ threshold is a function of θ_{sat} (degrees) and is given by Equation15.

$$\beta_{stropo}(12/11\mu m)_{threshold} = -0.01 * \theta_{sat} + 1.60 \quad \text{(Eq. 15)}$$

3.4.2.4.4 Multilayer Ash Confidence

An identical process is performed as described in sections 3.4.2.4.1 - 3.4.2.4.3, except multilayer β-ratios and cloud emissivities (section 3.4.2.1.2) are used instead of single layer β-ratios and cloud emissivities. When a 'Single_Layer' Ash Detection PQI Flag is referenced, the analogous 'Multi_Layer' flag should be used when calculating multilayer ash confidence. Additionally, Filter 1 of section 3.4.2.4.3 is not applied since no single/multiple layer information is used within that quality control filter. The resultant 'Summed Confidence' is known as 'Summed Multilayer Confidence', as to distinguish it from the single layer 'Summed Confidence'.

The 'Summed Confidence' and 'Summed Multilayer Confidence' (Ash QF Flags Ash_Single_Layer_Conf_Qf and Ash_Multi_Layer_Conf_Qf) are used within the retrieval algorithm to 1) determine what pixels to perform the retrieval and 2) whether single layer or multilayer assumptions should be made when performing the retrieval. Single layer assumptions are made within the retrieval unless the 'Summed Multilayer Confidence' is equal to "high" confidence for the pixel, then the pixel is considered multilayered and multilayer assumptions are used. When multilayered assumptions are used, the clear sky radiance term in the infrared radiative transfer equation (Equation 1) is replaced by the black cloud radiance term discussed in Section 3.4.2.1.2 and Section

3.4.2.1.4. For validation purposes, ash pixels are considered to be those with 'Summed Confidence' of "high" or "moderate" confidence or 'Summed Multilayer Confidence' of "high". The "low" and "very low" 'Summed Confidence' pixels and the "moderate", "low", and "very low" 'Summed Multilayer Confidence' pixels are still retrieved for users with a desire for more ash pixels at the expense of increased false alarm.

3.4.2.5 Noise Filtering of Ash Confidence

In an effort to eliminate isolated volcanic ash false alarms, the 'Summed Confidence' and 'Summed Multilayer Confidence' (which serve as a volcanic ash mask), constructed using the rules described in Section 3.4.2.4, is subjected to a standard median filter that is applied to 3 x 3 pixel arrays centered on the pixel of interest. The median filter simply replaces the value at each pixel with the median value of a 3 x 3 pixel array centered on that pixel. Figure 6 shows the impact of the median filter. The median filter is very effective at eliminating random incoherent false alarms, which are similar to "salt and pepper" noise. The generic median filter procedure is described in detail in the AIADD Document.

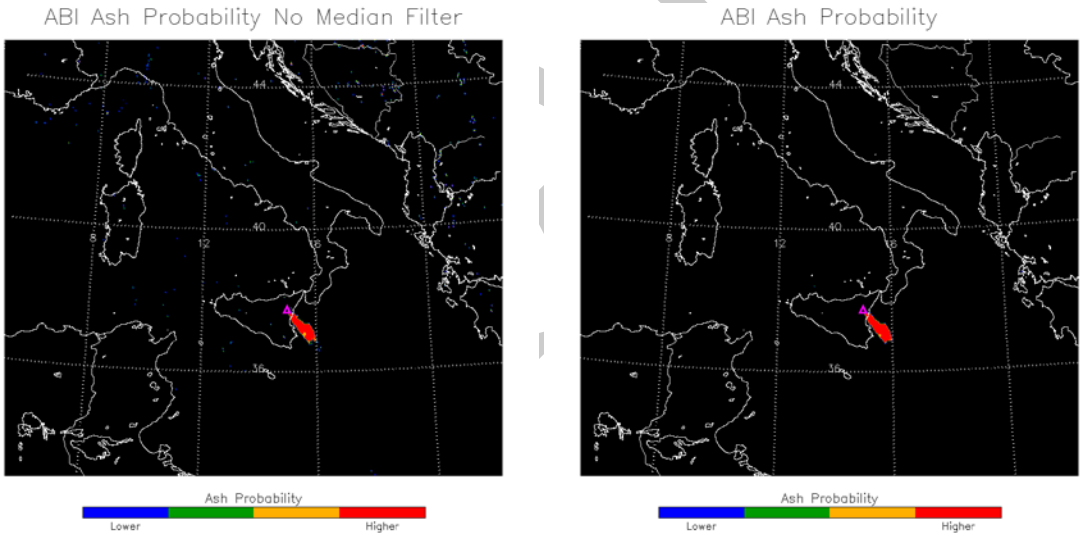

Figure 6: Volcanic ash confidence is shown for an eruption of Etna. The image on the left shows the results without the median filter applied. The image on the right shows the results with the median filter applied. The median filter eliminates isolated false alarms (blue speckles), while leaving the actual volcanic ash cloud in tact (orange/red feature).

3.4.2.6 Ash/Dust Discrimination

Figure 2 and Figure 3 show that volcanic rock and desert dust have similar spectral signatures in the 8 – 12 μm "window" while meteorological clouds have a different

spectral signature. While the algorithm successfully discriminates ash from most meteorological clouds, most airborne dust clouds will be detected by the volcanic ash detection scheme. The F&PS requirements state that an ash/dust discrimination scheme is not required, as the product statistics are only applicable to volcanic ash cases. Users should be aware that the GOES-R algorithm cannot reliably separate volcanic ash and dust.

3.4.3 Physics of the Problem – Volcanic Ash Retrieval

The volcanic ash retrieval algorithm utilizes ABI channels 14, 15, and 16 (11 μm, 12 μm, and 13.3 μm) (VIIRS channels 15 and 16 (11 and 12 μm)). These channels are referred to by their approximate central wavelengths (11 μm, 12 μm, and 13.3 μm) throughout this "Theoretical Description." The algorithm does not directly retrieve ash height or ash mass loading. It retrieves ash cloud effective temperature, effective emissivity, and a microphysical parameter. These retrieved parameters are then used to estimate the ash cloud height and mass loading.

3.4.3.1 Cloudy Radiative Transfer

Assuming a satellite viewing perspective (e.g. upwelling radiation), a fully cloudy field of view, a non-scattering atmosphere (no molecular scattering), and a negligible contribution from downwelling cloud emission or molecular emission that is reflected by the surface and transmitted to the top of troposphere (Zhang and Menzel (2002) showed that this term is very small at infrared wavelengths), the cloudy radiative transfer equation for a given infrared channel or wavelength can be written as in Equation 16 (e.g. Heidinger and Pavolonis, 2009).

$$R_{obs}(\lambda) = \varepsilon(\lambda)R_{ac}(\lambda) + t_{ac}(\lambda)\varepsilon(\lambda)B(\lambda, T_{eff}) + R_{clr}(\lambda)(1-\varepsilon(\lambda)) \quad \text{(Eq. 16)}$$

In Equation 16, λ is wavelength, R_{obs} is the observed radiance, R_{clr} is the clear sky radiance. R_{ac} and t_{ac} are the above cloud upwelling atmospheric radiance and transmittance, respectively. B is the Planck Function, and T_{eff} is the effective cloud temperature. The effective cloud emissivity (Cox, 1976) is given by ε. To avoid using additional symbols, the angular dependence is simply implied. While the above radiative transfer equation is simple in that it does not explicitly account for cloud scattering (cloud scattering is implicitly accounted for in the effective emissivity, see Cox, 1976) and that the cloud can be treated as a single layer, it does allow for semi-analytic derivations of the observations to the controlling parameters (i.e. cloud temperature). This is critical because it allows for an efficient retrieval without the need for large lookup tables.

Equation 16 can readily be solved for the effective cloud emissivity as follows:

$$\varepsilon(\lambda) = \frac{R_{obs}(\lambda) - R_{clr}(\lambda)}{[B(\lambda, T_{eff})t_{ac}(\lambda) + R_{ac}(\lambda)] - R_{clr}(\lambda)} \quad \text{(Eq. 17)}$$

In Equation 17, the term in brackets in the denominator is the blackbody cloud radiance that is transmitted to the top of atmosphere (TOA) plus the above cloud (ac) atmospheric radiance. This term is dependent upon the cloud vertical location.

In this retrieval algorithm, the effective cloud emissivity is allowed to vary spectrally. It is the spectral variation of the effective cloud emissivity that holds the cloud microphysical information (particle size, shape, and composition), which is important for calculating the ash mass loading. To account for this spectral variation, the effective cloud emissivity is used to calculate effective absorption optical depth ratios; otherwise known as β-ratios (see Inoue 1987; Parol et al., 1991; Giraud et al., 1997; and Heidinger and Pavolonis, 2009). For a given pair of spectral cloud emissivities ($\varepsilon(\lambda_1)$ and $\varepsilon(\lambda_2)$):

$$\beta_{obs} = \frac{\ln[1-\varepsilon(\lambda_1)]}{\ln[1-\varepsilon(\lambda_2)]} = \frac{\tau_{abs}(\lambda_1)}{\tau_{abs}(\lambda_2)} \quad \text{(Eq. 18)}$$

Notice that Equation 18 can simply be interpreted as the ratio of effective absorption optical depth (τ) at two different wavelengths or channels. Allowing the ash cloud microphysics to vary will also allow for improved estimates of ash cloud height as well.

An appealing quality of β_{obs}, is that it can be interpreted in terms of the single scatter properties, which can be computed for a given cloud composition and particle distribution. Following Van de Hulst (1980) and Parol et al. (1991), a spectral ratio of scaled extinction coefficients can be calculated from the single scatter properties (single scatter albedo, asymmetry parameter, and extinction cross section), as follows.

$$\beta_{theo} = \frac{[1.0 - \omega(\lambda_1)g(\lambda_1)]\sigma_{ext}(\lambda_1)}{[1.0 - \omega(\lambda_2)g(\lambda_2)]\sigma_{ext}(\lambda_2)} \quad \text{(Eq. 19)}$$

In Equation 19, β_{theo} is the spectral ratio of scaled extinction coefficients, ω is the single scatter albedo, g is the asymmetry parameter, and σ_{ext} is the extinction cross section. At wavelengths in the 8 – 15 μm range, where multiple scattering effects are small, β_{theo}, captures the essence of the cloudy radiative transfer such that,

$$\beta_{obs} \approx \beta_{theo} \quad \text{(Eq. 20)}$$

Equation 20, which was first shown to be accurate for observation in the 10 – 12 μm "window" by Parol et al. (1991), only depends upon the single scatter properties. This relationship is also verified in Pavolonis (2010a).

3.4.3.2 Microphysical Relationships

Since the ash retrieval utilizes three channels, two different β_{obs} are required to describe the spectral variation of cloud emissivity. Unfortunately, imager measurements do not contain enough information to retrieve more than one β_{obs}, so a pre-established relationship between the two β_{obs} must be used to constrain the retrieval problem. More specifically, the ash composition (e.g. the type of rock) and the ash particle habit (e.g. shape) must be assumed. This constraint, however, does not prevent the retrieval of quality ash particle size information. This pre-established relationship is derived from the corresponding spectral ratio of scaled extinction coefficients, as defined by Equation 19. All of the necessary microphysical assumptions are described below.

The volcanic ash particles are taken to be composed of andesite (Pollack et al, 1973). The size distribution was assumed to be lognormal. Lognormal distributions of andesite have been commonly used to model volcanic ash (e.g. Wen and Rose, 1994; Pavolonis et al., 2006; Prata and Grant, 2001). The andesite particles were assumed to be spherical and Mie theory is used to compute the single scatter properties. Of course, real volcanic ash particles actually take on a variety of irregular shapes that are very difficult to model, and the ash composition (e.g. the type of rock) varies from volcano to volcano. Fortunately, the sensitivity to particle habit and composition in the infrared is much smaller than the sensitivity to particle size (Wen and Rose, 1994). Given the composition and habit assumptions, the needed β relationship can be computed from the Mie generated single scatter properties. Figure 7 below shows the variation of the 11 and 12 μm β with the 11 and 13.3 μm β computed using Equation 19, where the 11 μm channel is always placed in the denominator of Equation 19. Hereafter, these β's are referred to as β(12/11μm) and β(13.3/11μm), respectively. In the retrieval, β(12/11μm) is a free parameter and β(13.3/11μm) is determined using the empirical relationship shown in Figure 7. The form of the empirical relationship is as follows.

$$\beta(13.3/11\mu m) = c4[\beta(12/11\mu m)]^4 + c3[\beta(12/11\mu m)]^3 + c2[\beta(12/11\mu m)]^2 + c1[\beta(12/11\mu m)] + c0$$
(Eq. 21)

The coefficients used in Equation 21 are listed as a function of sensor in Table 10.

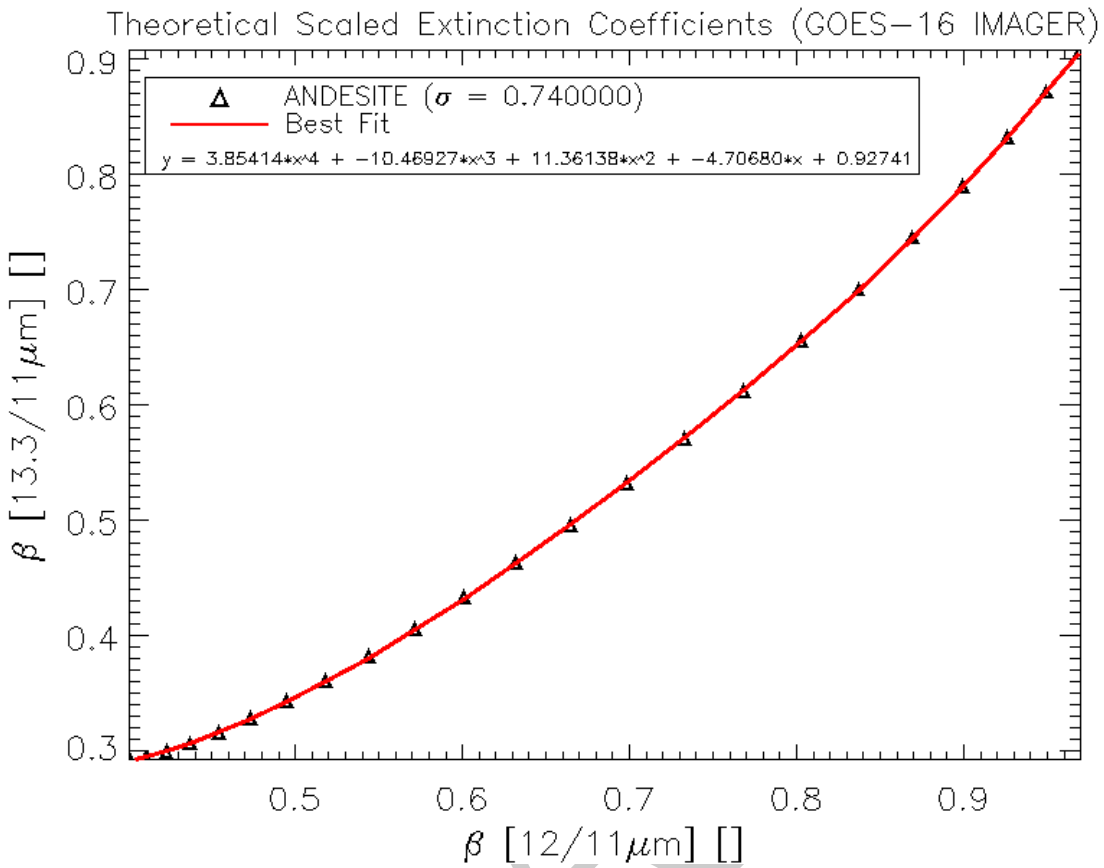

Figure 7: The 13.3/11 μm scaled extinction ratio (β(13.3/11 μm)) is shown as a function of the 12/11 μm scaled extinction ratio (β(12/11 μm)) for andesite spheres (volcanic ash). The andesite effective particle radius was varied from 1 to 13 μm, where larger values of β indicate larger particles. These β's were derived from single scatter properties calculated using Mie Theory and integrated over the corresponding ABI spectral response functions. The red line is the fourth degree polynomial fit.

Table 10: Regression coefficients needed to determine β(13.3/11μm) from β(12/11μm) using Equation 21. The coefficients are given as a function of sensor.

Sensor	C0	C1	C2	C3	C4
GOES-R ABI	0.92741	-4.70680	11.36138	-10.46927	3.85414
MET-8 SEVIRI	0.363415	-1.95058	6.22212	-6.67325	2.94788
MET-9 SEVIRI	0.307669	-1.57123	5.35150	-5.74824	2.57427
Terra MODIS	0.821825	-4.41789	11.0984	-10.8378	4.26339
Aqua MODIS	0.813096	-4.35587	10.9564	-10.6888	4.20431

Additional single scatter property based microphysical relationships are needed to convert the retrieved β(12/11μm) to an effective particle radius (r_{eff}) and the 11-μm extinction cross section (σ_{ext}(11μm)). Both of these parameters are needed when estimating the ash mass loading. Figure 8 and Figure 9 show the relationship used to convert the retrieved β(12/11μm) to an effective particle radius and extinction coefficient, respectively. The forms of these empirical relationships are as follows.

$$r_{eff} = \exp(c4[\beta(12/11\mu m)]^4 + c3[\beta(12/11\mu m)]^3 + c2[\beta(12/11\mu m)]^2 + c1[\beta(12/11\mu m)] + c0)$$

(Eq. 22)

$$\sigma_{ext}(11\mu m) = \exp(c4[\beta(12/11\mu m)]^4 + c3[\beta(12/11\mu m)]^3 + c2[\beta(12/11\mu m)]^2 + c1[\beta(12/11\mu m)] + c0)$$

(Eq. 23)

For notational convenience, generic symbols are used for the regression coefficients, which actually differ between Equations 21 - 23. The regression coefficients used in these expressions are given in Table 11 and Table 12 as a function of sensor.

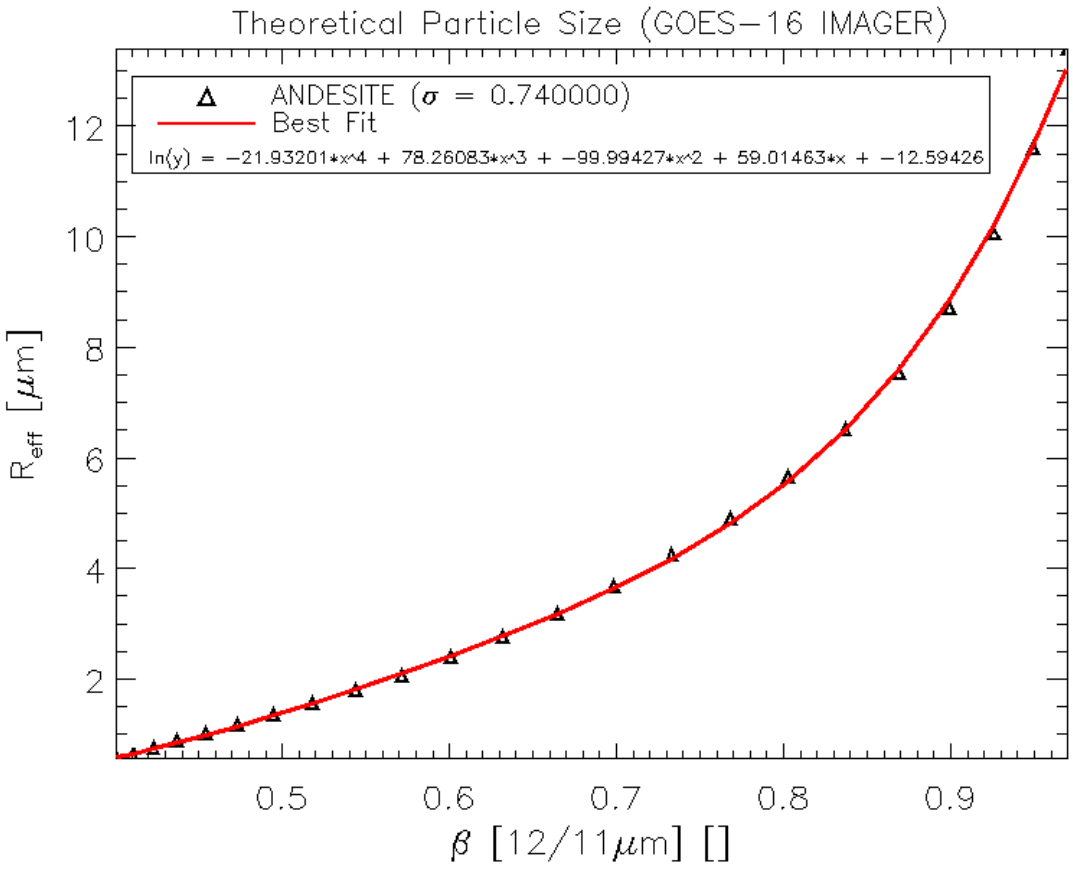

Figure 8: The effective particle radius is shown as a function of the 12/11 μm scaled extinction ratio (β(12/11 μm)) for andesite spheres (volcanic ash). The β(12/11 μm) was derived from single scatter properties calculated using Mie Theory and

integrated over the corresponding ABI spectral response functions. The red line is the fourth degree polynomial fit.

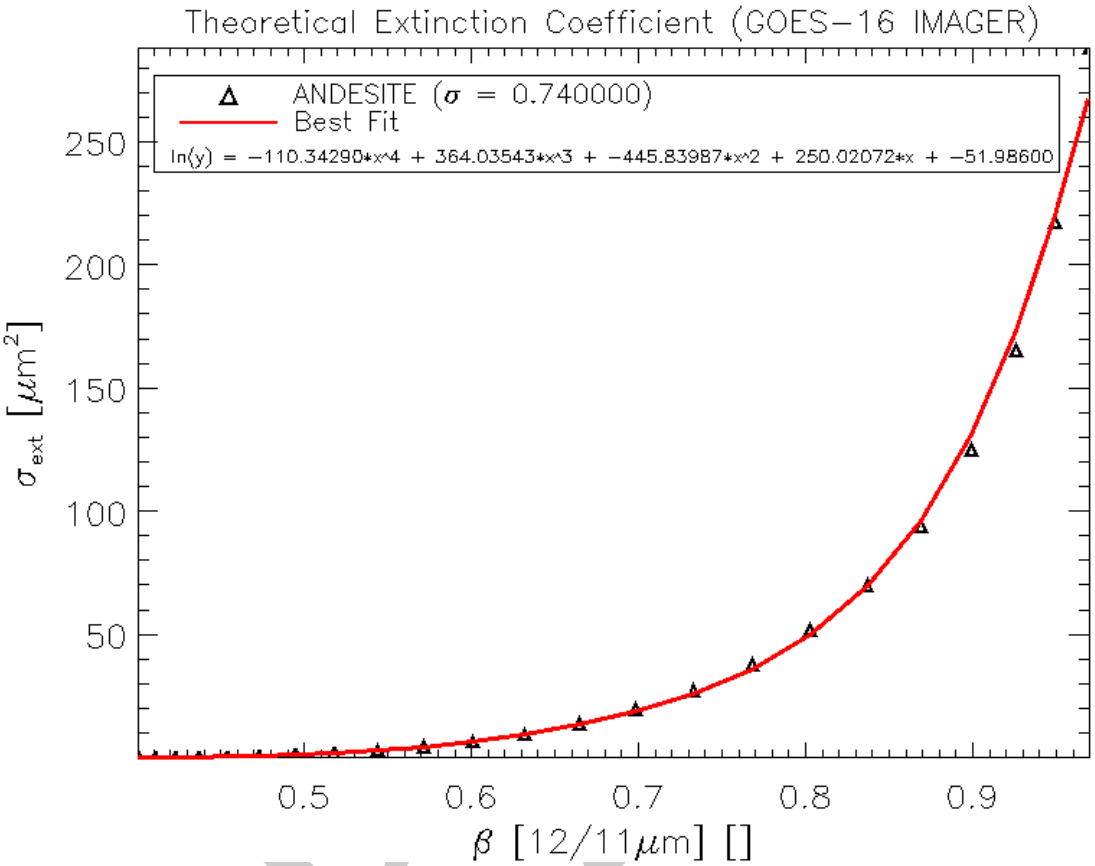

Figure 9: The extinction cross section is shown as a function of the 12/11 μm scaled extinction ratio (β(12/11 μm)) for andesite spheres (volcanic ash). The β(12/11 μm) was derived from single scatter properties calculated using Mie Theory and integrated over the corresponding ABI spectral response functions. The red line is the fourth degree polynomial fit.

Table 11: Regression coefficients needed to determine the effective particle radius in μm from β(12/11μm) using Equation 22. The coefficients are given as a function of sensor.

Sensor	C0	C1	C2	C3	C4
GOES-R ABI	-12.5943	59.0146	-99.9943	78.2608	-21.9320
MET-8 SEVIRI	-3.22925	10.6954	-5.17920	-5.68616	5.93906
MET-9 SEVIRI	-3.25818	11.8129	-8.69544	-1.56236	4.25769
Terra	-7.52014	30.9347	-42.0031	24.8926	-3.66602

MODIS					
Aqua MODIS	-7.52817	31.0711	-42.4260	25.4010	-3.87514

Table 12: Regression coefficients needed to determine the 11-μm extinction cross section in μm^2 from β(12/11μm) using Equation 23 are shown. The coefficients are given as a function of sensor.

Sensor	C0	C1	C2	C3	C4
GOES-R ABI	-51.9860	250.021	-445.840	364.035	-110.343
MET-8 SEVIRI	-13.2727	50.7207	-57.8280	25.4477	0.468358
MET-9 SEVIRI	-13.0247	52.3100	-64.7302	34.1704	-3.16255
Terra MODIS	-32.1321	141.961	-226.231	165.702	-43.5852
Aqua MODIS	-32.1062	142.052	-226.784	166.517	-43.9565

3.4.3.2.1 Microphysical Relationships – JPSS/VIIRS

This subsection supplements the parent subsection for JPSS/VIIRS microphysical relationships used in the physical retrieval, specifically a 2-channel retrieval compared to a 3-channel retrieval used for ABI-VAA.

Given the more limited spectral channel available from VIIRS, the physical retrieval is reduced to 2-channels. The retrieved parameters still include ash cloud effective temperature, effective emissivity, and a microphysical parameter. These retrieved parameters are then used to estimate the ash cloud height and mass loading. The microphysical relationships described by Equations 22 and 23 apply to VIIRS-VAA, Figure 10 and Figure 11, respectively. These figures show the relationship used to convert the retrieved β(12/11μm) to an effective particle radius and extinction coefficient, respectively. For notational convenience, generic symbols are used for the regression coefficients, which actually differ between Equations 22 and 23. The regression coefficients used in these expressions are given in Table 13 and Table 14.

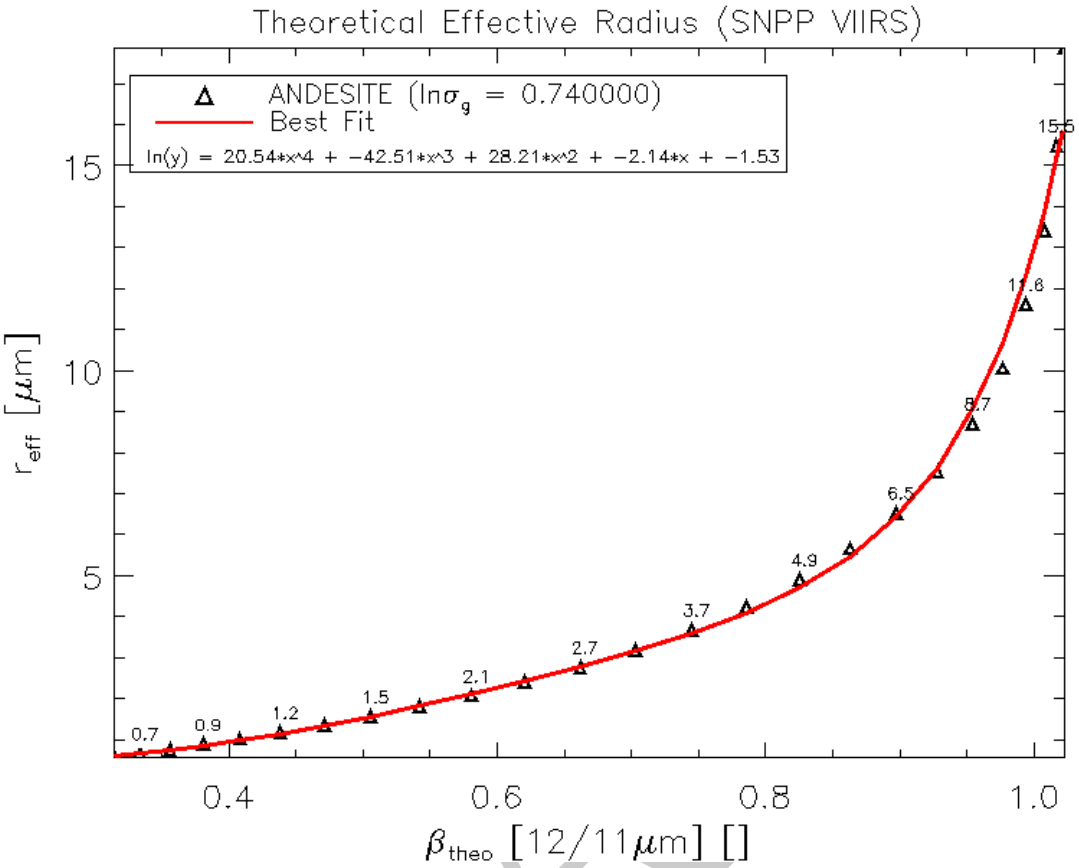

Figure 10: The effective particle radius is shown as a function of the 12/11 μm scaled extinction ratio (β(12/11 μm)) for andesite spheres (volcanic ash). The β(12/11 μm) was derived from single scatter properties calculated using Mie Theory and integrated over the corresponding VIIRS spectral response functions. The red line is the fourth degree polynomial fit.

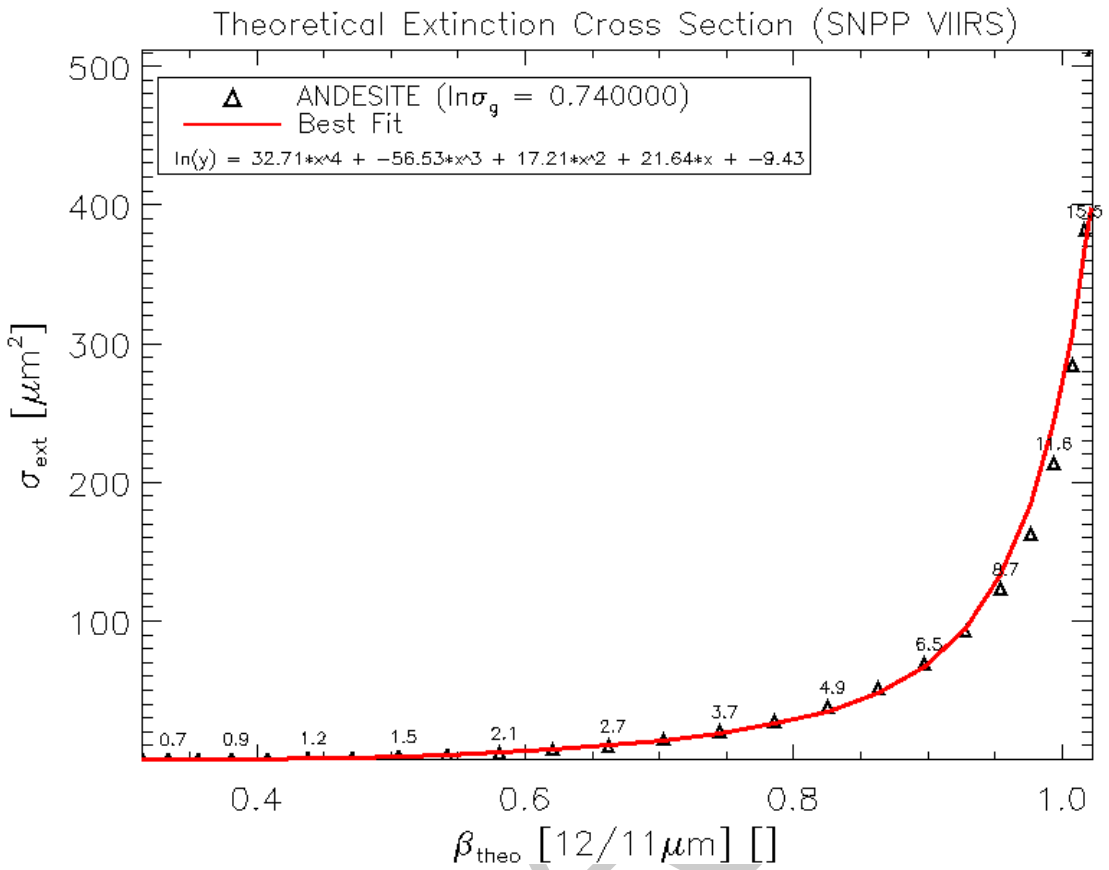

Figure 11: The extinction cross section is shown as a function of the 12/11 μm scaled extinction ratio (β(12/11 μm)) for andesite spheres (volcanic ash). The β(12/11 μm) was derived from single scatter properties calculated using Mie Theory and integrated over the corresponding VIIRS spectral response functions. The red line is the fourth degree polynomial fit.

Table 13: Regression coefficients needed to determine the effective particle radius in μm from β(12/11μm) using Equation 22. The coefficients are given as a function of sensor.

Sensor	C0	C1	C2	C3	C4
JPSS-VIIRS	-1.53	-2.14	28.21	-42.51	20.54

Table 14: Regression coefficients needed to determine the 11-μm extinction cross section in μm^2 from β(12/11μm) using Equation 23 are shown. The coefficients are given as a function of sensor.

Sensor	C0	C1	C2	C3	C4
JPSS-VIIRS	-9.43	21.64	17.21	-56.53	32.71

3.4.4 Mathematical Description

The mathematical approach employed here is the optimal estimation approach described by Rodgers (1976). The optimal estimation approach is also often referred to as a 1DVAR approach. The benefits of this approach are that it is flexible and allows for the easy addition or subtraction of new observations or retrieved parameters. Another benefit of this approach is that it generates automatic estimates of the retrieval errors. The optimal estimation approach minimizes a cost function, ϕ, given by

$$\phi = (x - x_a)^T S_a^{-1} (x - x_a) + (y - f(x))^T S_y^{-1} (y - f(x)) \quad \text{(Eq. 24)}$$

Where y is the vector of observations, x is the vector of retrieved parameters, f(x) represents the forward model, which is a function of x, and x_a is the *a priori* value of x. The matrices S_y and S_a are the error covariance matrices of the forward model and *a priori* values respectively. In our retrieval, the y, x, and x_a vectors are defined as follows.

$$y = \begin{pmatrix} BT(11\mu m) \\ BTD(11-12\mu m) \\ BTD(11-13.3\mu m) \end{pmatrix} \quad \text{(Eq. 25a)} \qquad x = \begin{pmatrix} T_{eff} \\ \varepsilon(11\mu m) \\ \beta(12/11\mu m) \end{pmatrix} \quad \text{(Eq. 25b)}$$

$$x_a = \begin{pmatrix} T_{eff}\_ap \\ \varepsilon(11\mu m)\_ap \\ \beta(12/11\mu m)\_ap \end{pmatrix} \quad \text{(Eq. 25c)}$$

The observation vector, y, consists of the 11 μm (ABI Channel 14, VIIRS Channel 15) brightness temperature (BT), the 11 minus 12 μm (ABI Channel 14 – Channel 15, VIIRS Channel 15 – Channel 16) brightness temperature difference (BTD) and the 11 – 13.3 μm (ABI Channel 14 – Channel 16) BTD *(ABI-VAA only)*. The use of BTD's is needed to capture the cloud microphysical signal. The retrieved parameters, x, are the effective cloud temperature (T_{eff}), the 11 μm cloud emissivity (ε(11μm)), and the 12/11 μm effective absorption optical depth ratio (β(12/11μm)). The symbols for the first guess or *a priori* estimates of the retrieved parameters are appended with "_ap." As explained earlier, these retrieved parameters are then used to estimate the ash cloud height and mass loading. The ash height and mass loading cannot be retrieved directly because they are not variables in the cloudy infrared radiative transfer equation.

3.4.4.1 Determining the *a priori* Values and Associated Uncertainty

The *a priori* values and their associated uncertainties act to constrain the retrieved parameters when the measurements contain little or no information on one or more of the retrieved parameters. The *a priori* error covariance matrix (Equation 26) is assumed to be diagonal (e.g. errors in the first guess of each parameter are uncorrelated). The *a*

priori values and their uncertainties depend on whether the ash cloud overlaps a lower meteorological cloud or if it is single layered, as determined by the volcanic ash detection routine. Table 15 shows the *a priori* values and their estimated uncertainties for both single and multilayered conditions. When forming the matrix given by Equation 26, the values in Table 15 need to be squared. These values were largely determined through analysis of semi-transparent ice clouds observed by spaceborne lidar (e.g. Heidinger and Pavolonis, 2009). Thus, these *a priori* estimates may not be ideal for volcanic ash clouds, but lidar observations of ash clouds are very rare, so better estimates are difficult to make. A large uncertainty is assigned to each *a priori* parameter, so that the measurements are given a high weight during the iteration. In summary, these values will likely be adjusted as more unique observations (e.g. lidar, in-situ, etc…) of volcanic ash clouds become available.

$$S_a = \begin{pmatrix} \sigma^2_{Teff\_ap} & 0.0 & 0.0 \\ 0.0 & \sigma^2_{\varepsilon(11\mu m)\_ap} & 0.0 \\ 0.0 & 0.0 & \sigma^2_{\beta(12/11\mu m)\_ap} \end{pmatrix} \quad \text{(Eq. 26)}$$

Table 15: The *a priori* (first guess) retrieval values used in the ABI volcanic ash retrieval. The T_{eff} first guess is a function of the 11 μm brightness temperature, B(11μm). The ε(11μm) first guess is a function of the satellite zenith angle, θ_{sat}.

Parameter	Single Layer *a priori*	Single Layer *a priori* Uncertainty	Multi-layer *a priori*	Multi-layer *a priori* Uncertainty
$\sigma_{Teff\ ap}$	BT(11μm) – 15 K	40 K	BT(11μm) – 15 K	40 K
$\sigma_{\varepsilon(11\mu m)\ ap}$	$1.0\text{-}e^{(-0.5/\cos(\theta_{sat}))}$	0.5	$1.0\text{-}e^{(-0.5/\cos(\theta_{sat}))}$	0.5
$\sigma_{\beta(12/11\mu m)\ ap}$	0.8	0.3	0.8	0.3

3.4.4.1.1 Determining the a priori Values and Associated Uncertainty – JPSS/VIIRS

This subsection supplements the parent subsection and reflects different *a priori* and uncertainty for the 2-channel retrieval used by the VIIRS-VAA.

Table 16: The *a priori* (first guess) retrieval values used in the ABI volcanic ash retrieval. The T_{eff} first guess is a function of the 11 μm brightness temperature, B(11μm). The ε(11μm) first guess is a function of the satellite zenith angle, θ_{sat}.

Parameter	Single Layer *a priori*	Single Layer *a priori* Uncertainty	Multi-layer *a priori*	Multi-layer *a priori* Uncertainty
$\sigma_{Teff\ ap}$	BT(11μm) – 10 K	10 K	BT(11μm) – 5 K	10 K

$\sigma_{\varepsilon(11\mu m)\ ap}$	$1.0\text{-}e^{(-0.5/\cos(\theta_{sat}))}$	0.7	$1.0\text{-}e^{(-0.5/\cos(\theta_{sat}))}$	0.5
$\sigma_{\beta(12/11\mu m)\ ap}$	0.8	0.2	0.8	0.2

3.4.4.2 The Forward Model

For notational convenience, we define the "blackbody" top-of-atmosphere cloud radiance, $R_{cld}(\lambda)$, as follows. All other terms in this equation have been defined previously.

$$R_{cld}(\lambda) = R_{ac}(\lambda) + t_{ac}(\lambda)B(\lambda, T_{eff}) \quad \text{(Eq. 27)}$$

Based on Equations 16 and 27, the radiance for each channel used in the retrieval is given by Equations 28 – 30. The Planck Function is then used to convert the radiances to brightness temperature, from which brightness temperature differences can be constructed.

$$R_{obs}(11\mu m) = \varepsilon(11\mu m)R_{cld}(11\mu m) + R_{clr}(11\mu m)(1-\varepsilon(11\mu m)) \quad \text{(Eq. 28)}$$

$$R_{obs}(12\mu m) = \varepsilon(12\mu m)R_{cld}(12\mu m) + R_{clr}(12\mu m)(1-\varepsilon(12\mu m)) \quad \text{(Eq. 29)}$$

$$R_{obs}(13.3\mu m) = \varepsilon(13.3\mu m)R_{cld}(13.3\mu m) + R_{clr}(13.3\mu m)(1-\varepsilon(13.3\mu m)) \quad \text{(Eq. 30) } \textit{(ABI-VAA only)}$$

The 12 and 13.3 μm cloud emissivities are not retrieved, so they must be determined at the beginning of each iteration in the optimal estimation scheme using ε(11μm), β(12/11μm), and Equation 21 (in the case of ε(13.3μm)) to evaluate the following relationships, which were derived from Equation 17.

$$\varepsilon(12\mu m) = 1-[1-\varepsilon(11\mu m)]^{\beta(12/11\mu m)} \quad \text{(Eq. 31)}$$

$$\varepsilon(13.3\mu m) = 1-[1-\varepsilon(11\mu m)]^{\beta(13.3/11\mu m)} \quad \text{(Eq. 32) } \textit{(ABI-VAA only)}$$

If the volcanic ash detection results indicate that an ash cloud likely overlaps a lower meteorological cloud, then the clear sky radiance, $R_{clr}(\lambda)$, in Equations 28 – 30 is replaced by the radiance from and above a black (emissivity = 1 at all wavelengths) elevated surface in an effort to account for the impact of the lower cloud layer. The mechanism used to compute the top-of-atmosphere radiance from and above the elevated black surface is described in detail in Section 3.4.2.1.

The errors associated with the forward model, f(x), must be characterized and expressed in the forward model error covariance matrix, S_y (Equation 33). The largest source of uncertainty in the forward model is the clear sky radiative transfer. The uncertainty in the clear sky radiative transfer should include the effects of errors in the surface temperature, surface emissivity, and atmospheric profiles. Spatial heterogeneity is another source of

error since the retrieval assumes that each pixel is uniformly cloudy. Instrumental issues, such as those due to calibration and noise effects, also contribute to the forward model error. Thus, the total uncertainty in the forward model is assumed to be composed of a linear combination of three major sources (see Equation 34): instrumental, clear sky radiative transfer modeling, and pixel heterogeneity. In Equation 34, the instrument uncertainty is given by σ^2_{instr}, the clear sky radiative transfer uncertainty is denoted by σ^2_{clr}, and the uncertainty due to pixel heterogeneity is given by σ^2_{hetero}. The impact of the clear sky radiative transfer uncertainty is approximately inversely proportional to the cloud emissivity, so it is weighted by the 11-μm cloud emissivity, ε(11μm). The off-diagonal elements (correlated uncertainty) of the forward model error covariance matrix are very difficult to determine, so only the diagonal elements (uncorrelated uncertainty) are considered.

$$S_y = \begin{pmatrix} \sigma^2_{BT(11\,\mu m)} & 0.0 & 0.0 \\ 0.0 & \sigma^2_{BTD(11-12\,\mu m)} & 0.0 \\ 0.0 & 0.0 & \sigma^2_{BTD(11-13.3\,\mu m)} \end{pmatrix} \quad \text{(Eq. 33)}$$

$$\sigma^2 = \sigma^2_{instr} + [1 - \varepsilon(11\mu m)]\sigma^2_{clr} + \sigma^2_{hetero} \quad \text{(Eq. 34)}$$

The uncertainty in the clear sky radiative transfer (σ^2_{clr}) is determined through a radiance bias analysis. The radiance bias estimates should be monitored over time and changes to σ^2_{clr} should be made accordingly. The current estimates of σ^2_{clr}, which are shown in Table 17, are based on analysis of Spinning Enhanced Visible and Infrared Imager (SEVIRI) data. These estimates will need to be updated during the early orbit period of the ABI as explained in detail in the ABI Volcanic Ash Product Validation Plan document. As expected, the uncertainty over land surfaces is larger than over open water. Over land, larger errors in surface temperature and surface emissivity results in larger radiance biases compared to water surfaces. It should be noted that the clear sky radiance biases will become smaller as clear sky radiative transfer models, numerical weather prediction models, and surface emissivity estimates improve.

The forward model uncertainty due to spatial heterogeneity (σ^2_{hetero}) is approximated by the variance of each observation used in the retrieval over a 3 x 3 pixel box centered on the current pixel of interest. The last and probably least significant forward model error term is that due to instrumental effects, σ^2_{instr}. This term includes noise, calibration, and spectral response errors. The current conservative estimates of this uncertainty are given in Table 17. Similar to the uncertainty estimates associated with the clear sky radiative transfer, these will need to be updated during the early orbit period.

Table 17: The individual components of the total forward model uncertainty used in the ABI volcanic ash retrieval. The total uncertainty is given by Equation 34. These values need to be squared when building the matrix given by Equation 33.

The University of Maryland surface type is used to distinguish between land and water.

Parameter	Instrument Uncertainty (σ_{instr})	Clear Sky Radiance Uncertainty (σ_{clr}) (Land, Water)	Non-uniform Pixel Uncertainty (σ_{hetero})
$\sigma_{BT(11\mu m)}$	0.25 K	5.0 K, 0.5 K	variable (see text)
$\sigma_{BTD(11\text{-}12\mu m)}$	0.25 K	1.0 K, 0.5 K	variable (see text)
$\sigma_{BTD(11\text{-}13.3\mu m)}$	0.5 K	4.0 K, 1.0 K	variable (see text)

3.4.4.2.1 The Forward Model – JPSS/VIIRS

This subsection supplements the parent subsection and reduces the description of the previous section to a 2-channel retrieval approach needed by the VIIRS-VAA.

The physical reasoning described in the preceding subsection applies to the VIIRS-VAA forward model, except fewer channels are used. Given the lack of 13.3 μm on VIIRS, Equations 30 and 32 are not applicable and Equation 33 is reduced by eliminating the bottom row and right most column to become a 2x2 matrix. The individual components of the total VIIRS-VAA forward model uncertainty are given in Table 18.

Table 18: The individual components of the total forward model uncertainty used in the VIIRS volcanic ash retrieval. The total uncertainty is given by Equation 34. These values need to be squared when building the matrix given by Equation 33. The University of Maryland surface type is used to distinguish between land and water.

Parameter	Instrument Uncertainty (σ_{instr})	Clear Sky Radiance Uncertainty (σ_{clr}) (Land, Water)	Non-uniform Pixel Uncertainty (σ_{hetero})
$\sigma_{BT(11\mu m)}$	0.50 K	5.0 K, 0.5 K	variable (see text)
$\sigma_{BTD(11\text{-}12\mu m)}$	0.25 K	1.0 K, 0.25 K	variable (see text)

3.4.4.3 Optimal Estimation Iterations

Each step in the optimal estimation iteration changes each element of x as governed by the following relationship

$$\delta x = S_x\{K^T S_y^{-1}[y - f(x)] + S_a^{-1}(x_a - x)\} \quad \text{(Eq. 35)}$$

where δx is the amount by which x is incremented during a given retrieval iteration and S_x is error covariance matrix of x and K is the Kernel or Jacobian matrix. The Kernel matrix contains the partial derivatives of each element of f to each element of x as

follows (*for VIIRS-VAA implementation, Kernel references to the 13.3 μm should be ignored).*

$$K = \begin{pmatrix} \frac{\partial BT(11\mu m)}{\partial T_{eff}} & \frac{\partial BT(11\mu m)}{\partial \varepsilon(11\mu m)} & \frac{\partial BT(11\mu m)}{\partial \beta(12/11\mu m)} \\ \frac{\partial BTD(11-12\mu m)}{\partial T_{eff}} & \frac{\partial BTD(11-12\mu m)}{\partial \varepsilon(11\mu m)} & \frac{\partial BTD(11-12\mu m)}{\partial \beta(12/11\mu m)} \\ \frac{\partial BTD(11-13.3\mu m)}{\partial T_{eff}} & \frac{\partial BTD(11-13.3\mu m)}{\partial \varepsilon(11\mu m)} & \frac{\partial BTD(11-13.3\mu m)}{\partial \beta(12/11\mu m)} \end{pmatrix} \quad \text{(Eq. 36)}$$

Given our choice of forward model, an analytical expression for each element of K can be derived from Equations 28 – 32, Equation 21, and the Planck Function. The derivative of each of the forward model simulated observations with respect to T_{eff} is given by the following set of equations. In these equations, $\partial B(\lambda)/\partial T_{eff}$ is the derivative of the Planck Function with respect to the effective cloud temperature, T_{eff}, and $\partial B(\lambda)/\partial T$ is the derivative of the Planck Function with respect to the forward model derived brightness temperature. All other symbols have been previously defined.

$$\frac{\partial BT(11\mu m)}{\partial T_{eff}} = \varepsilon(11\mu m) t_{\infty}(11\mu m) \left(\frac{\partial B(11\mu m)}{\partial T_{eff}}\right)\left(\frac{\partial B(11\mu m)}{\partial T}\right)^{-1} \quad \text{(Eq. 37)}$$

$$\frac{\partial BTD(11-12\mu m)}{\partial T_{eff}} = \frac{\partial BT(11\mu m)}{\partial T_{eff}} - \varepsilon(12\mu m) t_{\infty}(12\mu m) \left(\frac{\partial B(12\mu m)}{\partial T_{eff}}\right)\left(\frac{\partial B(12\mu m)}{\partial T}\right)^{-1} \quad \text{(Eq. 38)}$$

$$\frac{\partial BTD(11-13.3\mu m)}{\partial T_{eff}} = \frac{\partial BT(11\mu m)}{\partial T_{eff}} - \varepsilon(13.3\mu m) t_{\infty}(13.3\mu m) \left(\frac{\partial B(13.3\mu m)}{\partial T_{eff}}\right)\left(\frac{\partial B(13.3\mu m)}{\partial T}\right)^{-1} \quad \text{(Eq. 39)}$$

The following equations give the derivative of each forward model simulation with respect to ε(11μm).

$$\frac{\partial BT(11\mu m)}{\partial \varepsilon(11\mu m)} = [R_{cld}(11\mu m) - R_{clr}(11\mu m)]\left(\frac{\partial B(11\mu m)}{\partial T}\right)^{-1} \quad \text{(Eq. 40)}$$

$$\frac{\partial BTD(11-12\mu m)}{\partial \varepsilon(11\mu m)} =$$

$$\frac{\partial BT(11\mu m)}{\partial \varepsilon(11\mu m)} - [R_{cld}(12\mu m) - R_{clr}(12\mu m)][\beta(12/11\mu m)(1-\varepsilon(11\mu m))^{\beta(12/11\mu m)-1}]\left(\frac{\partial B(12\mu m)}{\partial T}\right)^{-1}$$

(Eq. 41)

$$\frac{\partial BTD(11-13.3\mu m)}{\partial \varepsilon(11\mu m)} =$$

$$\frac{\partial BT(11\mu m)}{\partial \varepsilon(11\mu m)} - [R_{cld}(13.3\mu m) - R_{clr}(13.3\mu m)][\beta(13.3/11\mu m)(1-\varepsilon(11\mu m))^{\beta(13.3/11\mu m)-1}]\left(\frac{\partial B(13.3\mu m)}{\partial T}\right)^{-1}$$

(Eq. 42)

Finally, the derivative of each forward model simulation with respect to β(12/11μm) is given by the following equations. In Equation 45, ∂β(13.3/11μm)/∂β(12/11μm) is applied to Equation 21 *(ABI-VAA only).*

$$\frac{\partial BT(11\mu m)}{\partial \beta(12/11\mu m)} = 0.0 \quad \text{(Eq. 43)}$$

$$\frac{\partial BTD(11-12\mu m)}{\partial \beta(12/11\mu m)} = [R_{cld}(12\mu m) - R_{clr}(12\mu m)]\ln[1-\varepsilon(11\mu m)][1-\varepsilon(12\mu m)]\left(\frac{\partial B(12\mu m)}{\partial T}\right)^{-1}$$

(Eq. 44)

$$\frac{\partial BTD(11-13.3\mu m)}{\partial \beta(12/11\mu m)} =$$

$$[R_{cld}(13.3\mu m) - R_{clr}(13.3\mu m)]\ln[1-\varepsilon(11\mu m)][1-\varepsilon(13.3\mu m)]\left(\frac{\partial \beta(13.3/11\mu m)}{\partial \beta(12/11\mu m)}\right)\left(\frac{\partial B(13.3\mu m)}{\partial T}\right)^{-1}$$

(Eq. 45)

Once the Kernel Matrix has been calculated, the error covariance matrix of x (Equation 46) can be determined using Equation 47 (Rodgers, 1976).

$$S_x = \begin{pmatrix} \sigma^2_{Teff} & 0.0 & 0.0 \\ 0.0 & \sigma^2_{\varepsilon(11\mu m)} & 0.0 \\ 0.0 & 0.0 & \sigma^2_{\beta(12/11\mu m)} \end{pmatrix} \quad \text{(Eq. 46)}$$

$$S_x = (S_a^{-1} + K^T S_y^{-1} K)^{-1} \quad \text{(Eq. 47)}$$

The optimal estimation approach is run until the following convergence criterion is met.

$$\left\| \sum \delta x S_x^{-1} \delta x \right\| \le \frac{p}{2} \quad \text{(Eq. 48)}$$

Where p is the size of x, which is 3 in our case. This convergence criterion is taken out of Rodgers (1976). If the retrieval does not converge after 10 iterations, it is deemed a failed retrieval. In the event of a failed retrieval, all retrieved parameters are set to missing, not the *a priori* values. The *a priori* values are not used since ash cloud properties are highly variable in time and space and cannot be accurately parameterized by guess values alone. Very few retrievals (< 0.01%) fail to converge, so this has a negligible impact on the ash products. Further, δx is constrained such that the maximum allowed absolute changes in the retrieved parameters, T_{eff}, ε(11μm), and β(12/11μm), are

20.0 K, 0.3, 0.2, respectively. Once the retrieval vector is updated by δx, the retrieved parameters are constrained to be within a certain physically based range. Table 19 shows the allowed min and max values of each retrieved parameter.

Table 19: The valid range for each retrieved parameter.

Parameter	Minimum Allowed Value	Maximum Allowed Value
T_{eff}	160 K	330 K
ε(11μm)	0.0	1.0
β(12/11μm)	0.20	1.05

3.4.4.4 Retrieval Quality Flags

The actual retrieval error estimates are given by the square root of the diagonal elements of S_x. The information from these error estimates is packed into a quality flag for each parameter by comparing the error in the retrievals to the uncertainty of the *a priori* estimates using the following logic.

Quality is judged based on how much the first guess is improved (or not). The highest quality is assigned to a given retrieved parameter when $S_x(n,n) < 0.111*S_a(n,n)$, where n is the index of the retrieved parameter. Intermediate quality is assigned to a given retrieved parameter when $0.111*S_a(n,n) \leq S_x(n,n) < 0.444*S_a(n,n)$. The lowest quality is assigned when $S_x(n,n) \geq 0.444*S_a(n,n)$. The factors 0.111 and 0.444 correspond to the square root of 1/3 and 2/3, respectively.

3.4.4.5 Computation of Cloud Height

The retrieved T_{eff} is used to estimate the ash cloud height. First, linear interpolation weights and anchor points are determined by locating T_{eff} within the NWP temperature profile. The temperature profile is searched from high to low vertical levels. The vertical NWP profiles used in the ash retrievals are cropped to only use levels between the surface and model tropopause. The weights and anchor points are then used to determine the ash cloud height. Equation 49 illustrates the interpolation technique. In Equation 49, Z_{ash} is the ash cloud height. T1 and T2 are the temperatures within the profile that bound T_{eff}, with T1 being the temperature at the highest (e.g. furthest from the ground) bounding level. Z1 and Z2 are the corresponding height of the bounding temperatures, T1 and T2.

$$Z_{ash} = Z1 + \left(\frac{T_{eff} - T1}{T2 - T1}\right)(Z2 - Z1) \quad \text{(Eq. 49)}$$

3.4.4.6 Computation of Ash Mass Loading

The method for computing ash mass loading is based on the methodology used by Zhang et al. (2006). The ash mass loading is computed from the retrieved 11-μm cloud

emissivity ($\varepsilon(11\mu m)$) and the retrieved $\beta(12/11\ \mu m)$. First, the effective 11-μm emissivity is converted to an effective optical depth, $\tau(11\mu m)$, using:

$$\tau(11\mu m) = -\cos(\theta_{sat})\ln[1.0 - \varepsilon(11\mu m)] \quad \text{(Eq. 50)}$$

In Equation 50, θ_{sat} is the satellite zenith angle. The mass loading (and effective radius) computations described below are only performed if $\beta(12/11\ \mu m) > 0.0$ and $\tau(11\mu m) > 0.0$. If those conditions are true, next, the retrieved $\beta(12/11\ \mu m)$ is used to determine the effective particle radius (r_{eff}) and the 11-μm extinction cross-section ($\sigma_{ext}(11\mu m)$) by applying the regression relationships given by Equations 22 and 23.

As described in Section 3.4.3.2, the ash distribution is assumed to be lognormal. Lognormal distributions have the following form.

$$n(r) = \frac{N_o}{\sqrt{2\pi}} \frac{1}{r \ln \sigma} e^{\left[-\frac{(\ln r - \ln r_{mod})^2}{2(\ln \sigma)^2}\right]} \quad \text{(Eq. 51)}$$

In Equation 51, n(r) is the number particles per unit area per bin of particle size. From an implementation standpoint, n(r) is constructed using values of r that range from 0.10 μm to 100.0 μm in 0.10 μm increments. N_o is the total number of particles per unit area, r is the particle radius, r_{mod} is the modal radius, and σ is the width parameter of the lognormal distribution which is taken to be 0.74 (Wen and Rose, 1994). The modal radius, r_{mod} is calculated from the effective radius, r_{eff}.

$$r_{mod} = \frac{r_{eff}}{e^{\left[\frac{5}{2}(\ln \sigma)^2\right]}} \quad \text{(Eq. 52)}$$

The total number of particles per unit area is determined from the 11-μm cloud optical depth and the 11-μm extinction cross section using Equation 53.

$$N_o = \frac{\tau(11\mu m)}{\sigma_{ext}(11\mu m)} \quad \text{(Eq. 53)}$$

Finally, the mass loading is computed using:

$$ML = (1 \times 10^6)\left[\frac{4}{3}\pi\rho_{ash}\int_{r_1}^{r_2} r^3 n(r)\,dr\right](1x10^{-6}) \quad \text{(Eq. 54)}$$

In Equation 54, ML is the mass loading in tons/km^2 and ρ_{ash} is the density of ash, which is taken to be 2.6 g/cm^3 (Neal et al., 1994). The particle radius, r, is expressed in units of μm. The units of n(r) are the number of particles per μm^2 per μm. The factor, 1x10^6, in Equation 54, is needed to convert the units to tons/km^2. The integral in Equation 54 is numerically evaluated using rectangle rule quadrature.

3.4.5 Algorithm Output

3.4.5.1 Product Output

The ABI Volcanic Ash Algorithm produces the following products listed in the F&PS.

- Ash cloud height [km]
- Ash mass loading [tons/km^2]

The above products are derived at the pixel level for all pixels that potentially contain volcanic ash. For pixels that do not contain volcanic ash, the ash cloud height will be set to missing (-999.0) and the ash mass loading will be set to 0.0. When the ash retrieval fails, which is very rare, both the ash height and ash mass loading will be set to missing (-999.0). Example ash cloud height and ash mass loading output are shown in Figure 15.

3.4.5.2 Quality Flag (QF) Output

The ABI Volcanic Ash Algorithm produces quality flags. Table 20 describes the ash detection QF flags and **Table 21** describes the ash retrieval quality flags.

Byte	Bit	Name	Values	ATBD Section
1	1	Overall QF	0 – High Quality **1 – Low Quality**	3.4.2.4, Main Text
1	2	Invalid Data QF	0 – High Quality **1 – Low Quality**	3.4.2.4, Main Text
1	3	SatZenith QF	**0 – High Quality** 1 – Low Quality	3.4.2.4, Main Text
1	4-6	Ash Single Layer Confidence QF	0 – High 1 – Moderate 2 – Low 3 – Very Low **4 – Not-Ash**	3.4.2.4, Main Text
1	7-8	Spare	n/a	n/a
2	1-3	Ash Multi Layer Confidence QF	0 – High 1 – Moderate 2 – Low 3 – Very Low **4 – Not-Ash**	3.4.2.4, Main Text

Table 20: Ash Detection Quality Flag (QF) description. The Ash Detection QF Flags are bit packed byte variables. The byte column identifies the byte number(s) the QF is stored in and the Bit column lists the bit(s) the flag encompasses within the byte(s). The name of the each flag is included, along with possible values; the bold values are the initialized values. The ATBD section refers to the section where the test is described; where applicable additional text refers to specific location.

Byte	Bit	Name	Values	ATBD Section
1	1-2	Retrieval Status	0 - Successful 1 - Failed 2 - Not Attempted	n/a
1	3-4	T_{cld} QF	0 – High Quality 1 – Medium Quality 2 – Low Quality	3.4.4.4, Main Text
1	5-6	ε_{cld} QF	0 – High Quality 1 – Medium Quality 2 – Low Quality	3.4.4.4, Main Text
1	7-8	β(12/11μm) QF	0 – High Quality 1 – Medium Quality 2 – Low Quality	3.4.4.4, Main Text
2	1-4	Ash Particle Size	0 – ≥0 – < 2 μm 1 – ≥2 – < 3 μm 2 – ≥3 – < 4 μm 3 – ≥4 – < 5 μm 4 – ≥5 – < 6 μm 5 – ≥6 – < 7 μm 6 – ≥7 – < 8 μm 7 – ≥8 – < 9 μm 8 – ≥9 – < 10 μm 9 – ≥ 10 μm 10 - invalid	3.4.4.6, Main Text
2	5-8	Spare	n/a	n/a

Table 21: Ash Retrieval Quality Flag (QF) description. The Ash Retrieval QF Flags are bit packed byte variables. The byte column identifies the byte number(s) the QF is stored in and the Bit column lists the bit(s) the flag encompasses within the byte(s). The name of the each flag is included, along with possible values. The ATBD section refers to the section where the test is described; where applicable additional text refers to specific location.

3.4.5.3 Product Quality Information (PQI)

The ABI Volcanic Ash Algorithm Product Quality Informarion (PQI). Table 22 describes the ash detection Product Quality Information (PQI) and Table 23 describes the ash retrieval PQI.

Byte	Bit	Name	Values	ATBD Section
1	1	Strong_Btd_Weak_So2_Single_Layer	**0 – False** 1 – True	3.4.2.4.2, Rule 1
1	2	Strong_Btd_Weak_So2_Multi_Layer	**0 – False** 1 – True	3.4.2.4.2, Rule 1
1	3	Strong_Btd_Weak_So2_Inc_Conf_Single_Layer	**0 – False** 1 – True	3.4.2.4.2, Rule 2
1	4	Strong_Btd_Weak_So2_Inc_Conf_Multi_Layer	**0 – False** 1 – True	3.4.2.4.2, Rule 2

1	5	Weak_Btd_Strong_So2_Single_Layer	**0 – False** 1 – True	3.4.2.4.2, Rule 1
1	6	Weak_Btd_Strong_So2_Multi_Layer	**0 – False** 1 – True	3.4.2.4.2, Rule 1
1	7	Weak_Btd_Strong_So2_Inc_Conf_Single_Layer	**0 – False** 1 – True	3.4.2.4.2, Rule 3
1	8	Weak_Btd_Strong_So2_Inc_Conf_Multi_Layer	**0 – False** 1 – True	3.4.2.4.2, Rule 3
2	1	Remain_So2_Pixels_Single_Layer	**0 – False** 1 – True	3.4.2.4.2, Rule 4
2	2	Remain_So2_Pixels_Multi_Layer	**0 – False** 1 – True	3.4.2.4.2, Rule 4
2	3	Weak_Btd_Inc_Conf_Single_Layer	**0 – False** 1 – True	3.4.2.4.2, Rule 5
2	4	Weak_Btd_Inc_Conf_Multi_Layer	**0 – False** 1 – True	3.4.2.4.2, Rule 5
2	5	Strong_Btd_Inc_Conf_Single_Layer	**0 – False** 1 – True	3.4.2.4.2, Rule 6
2	6	Strong_Btd_Inc_Conf_Multi_Layer	**0 – False** 1 – True	3.4.2.4.2, Rule 6
2	7	Btd_Sw_Sfc_Emiss_Restoral	**0 – False** 1 – True	3.4.2.4.3, Rule 1
2	8	Low_Emiss_Filter_Single_Layer	**0 – False** 1 – True	3.4.2.4.3, Rule 2
3	1	Low_Emiss_Filter_Multi_Layer	**0 – False** 1 – True	3.4.2.4.3, Rule 2
3	4	Ice_Cloud_Filter_Single_Layer	**0 – False** 1 – True	3.4.2.4.3, Rule 3
3	5	Ice_Cloud_Filter_Multi_Layer	**0 – False** 1 – True	3.4.2.4.3, Rule 3
3	2	View_Angle_Filter_Single_Layer	**0 – False** 1 – True	3.4.2.4.3, Rule 4
3	3	View_Angle_Filter_Multi_Layer	**0 – False** 1 – True	3.4.2.4.3, Rule 4
3	6	Spectral_Tests_Attemped_Single_Layer	**0 – False** 1 – True	3.4.2.4.1, Rule 1
3	7	Spectral_Tests_Attempted_Multi_Layer	**0 – False** 1 – True	3.4.2.4.1, Rule 1
3	8	Valid_Lrc	**0 – False** 1 – True	3.4.2.3, Main Text
4	1-3	Ash_Pixel_Single_Layer	0 – High 1 – Moderate 2 – Low 3 – Very Low **4 – Not-Ash**	3.4.2.4.1, Rule 2
4	4-6	Ash_Lrc_Single_Layer	0 – High 1 – Moderate 2 – Low 3 – Very Low **4 – Not-Ash**	3.4.2.4.1, Rule 3
4	7-8	Spare	n/a	n/a
5	1-3	Ash_Pixel_Multi_Layer	0 – High 1 – Moderate 2 – Low 3 – Very Low	3.4.2.4.1, Rule 2

			4 – Not-Ash	
5	4-6	Ash_Lrc_Multi_Layer	0 – High 1 – Moderate 2 – Low 3 – Very Low **4 – Not-Ash**	3.4.2.4.1, Rule 3
5	7-8	Spare	n/a	n/a
6	1-3	Ash_Index_Init_Single_Layer	0 – High 1 – Moderate 2 – Low 3 – Very Low **4 – Not-Ash**	3.4.2.4.1, Rule 4
6	4-6	Ash_Index_Init_Multi_Layer	0 – High 1 – Moderate 2 – Low 3 – Very Low **4 – Not-Ash**	3.4.2.4.1, Rule 4

Table 22: Ash Detection PQI Flag description. The Ash Detection PQI Flags are bit packed byte variables. The byte column identifies the byte number(s) the PQI is stored in and the Bit column lists the bit(s) the flag encompasses within the byte(s). The name of the each flag is included, along with possible values; the bold values are the initialized values. The ATBD section refers to the section where the test is described; addition text refers to the specific rule/section within the listed section.

Byte	Bit	Name	Values	ATBD Section
1	1-2	Retrieval Status	0 - Successful 1 - Failed 2 - Not Attempted	n/a
1	3-4	Multilayer Retrieval	0 – No Ash 1 – Single Layer 2 – Multi Layer	3.4.2.4.4, Main Text
1	5-7	Microphysical Model Used	0 – No Model 1 – Andesite Log Sigma QP74 2 – Quartz Log Sigma QP74 3 – Kaolinite Log Sigma QP74 4 – Gypsum Log Sigma QP74	3.4.3.2, Main Text
1	8	Spare	n/a	n/a

Table 23: Ash Retrieval PQI Flag description. The Ash Retrieval PQI Flags are bit packed byte variables. The byte column identifies the byte number(s) the PQI is stored in and the Bit column lists the bit(s) the flag encompasses within the byte(s). The name of the each flag is included, along with possible values. The ATBD section refers to the section where the test is described; where applicable additional text refers to specific location.

3.4.5.4 Metadata

The metadata produced by the ABI-VAA are described in Table 24.

Metadata Output
Total mass of volcanic ash in scene
Mean ash mass loading in scene
Minimum ash mass loading value in scene
Maximum ash mass loading value in scene
Standard deviation of mass loading in scene
Minimum ash cloud height in scene
Maximum ash cloud height in scene
Mean ash cloud height in scene
Standard deviation of ash cloud height in scene
Total number of each T_{cld} QF flag value
Total number of each ε_{cld} QF flag value
Total number of each $\beta(12/11\mu m)$ QF flag value
Total number of each overall ash detection QF flag value
Total number of attempted ash retrievals in scene

Table 24: Ash algorithm metadata output.

4 Test Data Sets and Outputs

4.1 Simulated/Proxy Input Data Sets

As described below, the data used to test the ABI Volcanic Ash Algorithm (ABI-VAA) and VIIRS-VAA consists of Spinning Enhanced Visible and Infrared Imager (SEVIRI) and Moderate Resolution Imaging Spectrometer (MODIS) observations. SEVIRI and MODIS has observed several volcanic ash clouds. Given its coverage of the Sahara Desert, SEVIRI also commonly observes dust clouds. Dust is spectrally similar to volcanic ash in the infrared (see Figure 2 and Figure 3), so it can also be used to test the ash algorithms. In addition, several ash and dust free scenes were processed as a way of assessing the false alarm rate of the ash detection algorithm. The rest of this section describes the proxy and validation data sets used in assessing the performance of the ABI-VAA.

4.1.1 SEVIRI Data

SEVIRI provides 11 spectral channels with a spatial resolution of 3 km and provides spatial coverage of the full disk with a temporal resolution of 15 minutes. SEVIRI is a

good proxy source for testing and developing the ABI-VAA. The SEVIRI to ABI channel mapping is shown in **Table 25** and SEVIRI to VIIRS channel mapping is shown in **Table 26**. Figure 12, shown below, is a full-disk SEVIRI image from 12 UTC on November 24, 2006. SEVIRI data are readily available from the University of Wisconsin Space Science and Engineering Center (SSEC) Data Center.

SEVIRI Band Number	SEVIRI Wavelength Range (μm)	SEVIRI Central Wavelength (μm)	ABI Band Number	ABI Wavelength Range (μm)	ABI Central Wavelength (μm)
6	6.85 – 7.85	7.30	10	7.30 – 7.50	7.40
7	8.30 – 9.10	8.70	11	8.30 – 8.70	8.50
9	9.80 – 11.80	10.80	14	10.80 – 11.60	11.20
10	11.00 – 13.00	12.00	15	11.80 – 12.80	12.30
11	12.40 – 14.40	13.40	16	13.00 – 13.60	13.30

Table 25: The SEVIRI bands used to test the ABI volcanic ash algorithm is shown relative to the corresponding ABI bands.

SEVIRI Band Number	SEVIRI Wavelength Range (μm)	SEVIRI Central Wavelength (μm)	VIIRS Band Number	VIIRS Wavelength Range (μm)	VIIRS Central Wavelength (μm)
7	8.30 – 9.10	8.70	M14	8.4 – 8.7	8.55
9	9.80 – 11.80	10.80	M15	10.26 – 11.26	10.763
10	11.00 – 13.00	12.00	M16	11.54 – 12.49	12.013

Table 26: The SEVIRI bands used to test the VIIRS volcanic ash algorithm is shown relative to the corresponding VIIRS bands.

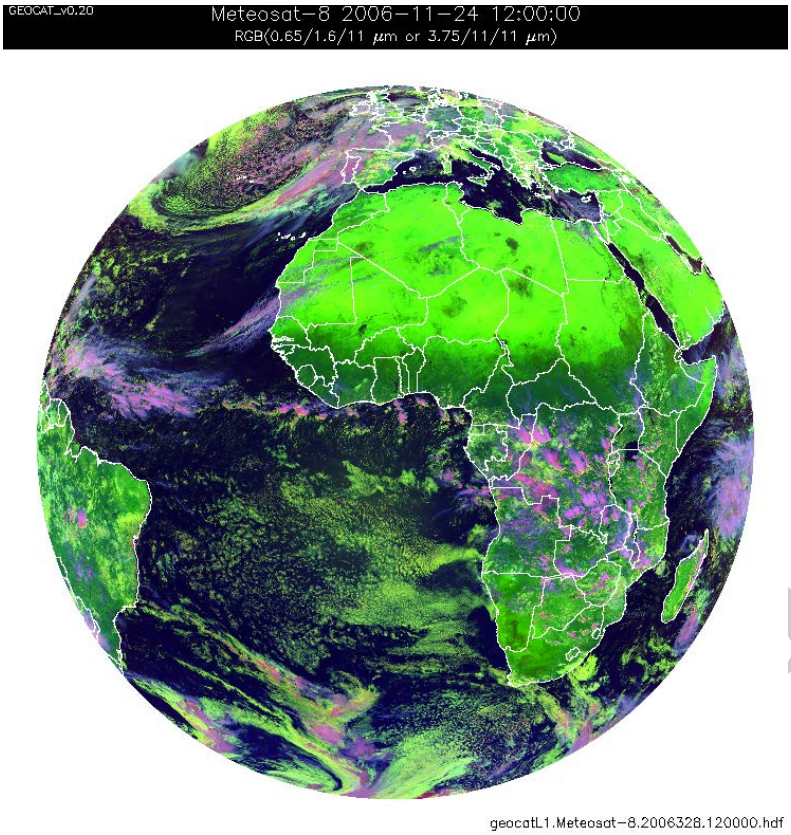

Figure 12: SEVIRI RGB image from 12 UTC on November 24, 2006.

4.1.2 MODIS Data

MODIS provides 36 spectral channels with a spatial resolution of 1 km and provides global coverage in low Earth orbit. MODIS on the Aqua spacecraft flies in the EOS A-Train, along with CALIPSO. The co-location of these spacecraft in the EOS A-Train provides time and space matchups of ash cloud and dust cloud observations over the entire globe. These data are utilized to validate the ash height and mass-loading algorithm. The MODIS to ABI channel mapping is shown in ***Table 27*** and MODIS TO VIIRS channel mapping is shown in ***Table 28***. An example MODIS false color image is shown in *Figure 13*.

MODIS Band Number	MODIS Wavelength Range (μm)	MODIS Central Wavelength (μm)	ABI Band Number	ABI Wavelength Range (μm)	ABI Central Wavelength (μm)
28	7.175 – 7.475	7.325	10	7.30 – 7.50	7.40
29	8.400 – 8.700	8.550	11	8.30 – 8.70	8.50
31	10.780 – 11.280	11.03	14	10.80 – 11.60	11.20

32	11.770 – 12.270	12.02	15	11.80 – 12.80	12.30
33	13.185 – 13.485	13.34	16	13.00 – 13.60	13.30

Table 27: The MODIS bands used to test the ABI volcanic ash algorithm is shown relative to the corresponding ABI bands.

MODIS Band Number	MODIS Wavelength Range (μm)	MODIS Central Wavelength (μm)	VIIRS Band Number	VIIRS Wavelength Range (μm)	VIIRS Central Wavelength (μm)
29	8.400 – 8.700	8.550	M14	8.4 – 8.7	8.55
31	10.780 – 11.280	11.03	M15	10.26 – 11.26	10.763
32	11.770 – 12.270	12.02	M16	11.54 – 12.29	12.013

Table 28: The MODIS bands used to test the VIIRS volcanic ash algorithm is shown relative to the corresponding VIIRS bands.

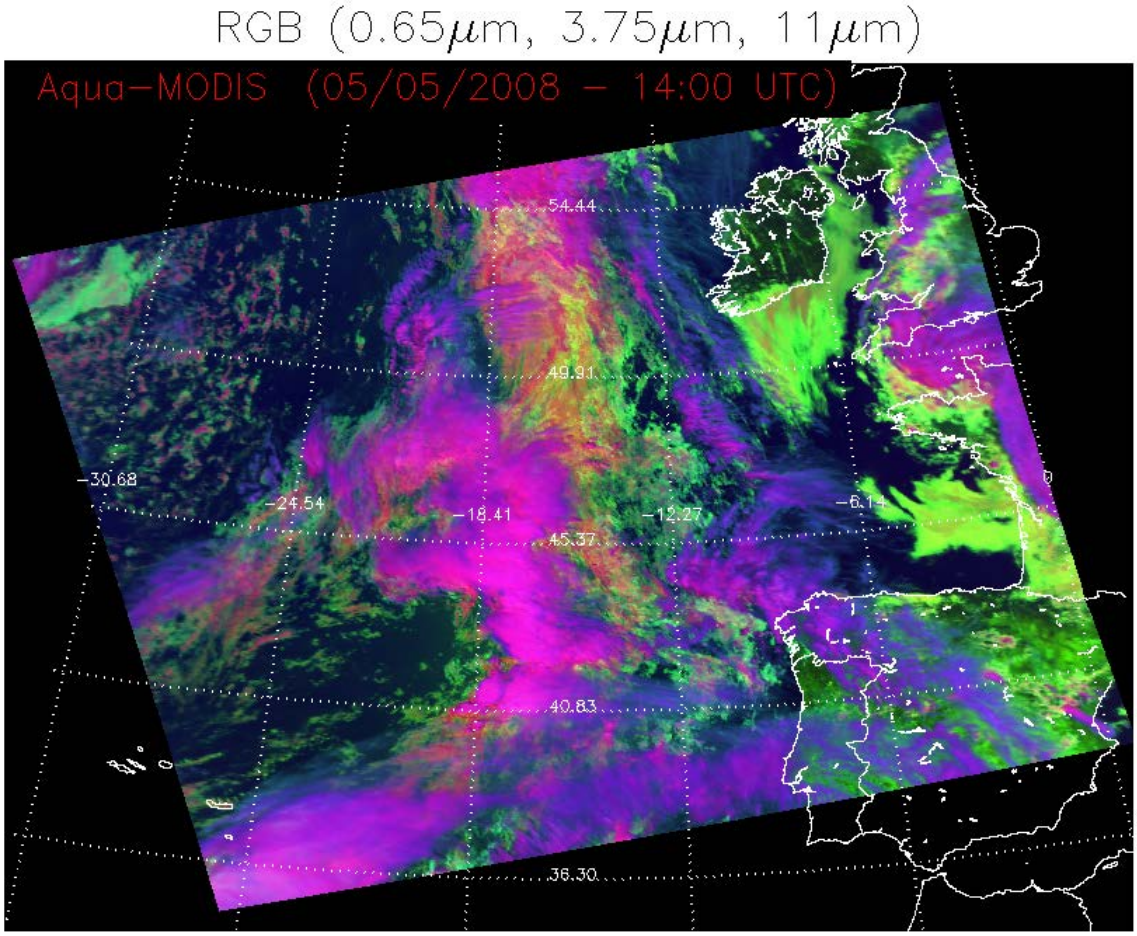

Figure 13: MODIS RGB image from 14 UTC on May 5, 2008.

4.1.3 CALIOP Data

With the launch of the Cloud-Aerosol Lidar and Infrared Pathfinder Satellite Observation (CALIPSO) into the EOS A-train in April 2006, the ability to validate satellite-based cloud and aerosol products increased significantly. The Cloud-Aerosol Lidar with Orthogonal Polarization (CALIOP) on-board the CALIPSO satellite is a dual wavelength depolarization lidar. We will primarily use the CALIOP cloud layer results to validate the volcanic ash height and mass loading products. The horizontal resolution of the CALIOP cloud layer data used in the validation is 1-km. An example 1-km CALIOP cross section is shown in Figure 14. All of the validation data sources and procedures, including CALIOP, are described in detail the ABI Volcanic Ash Product Validation Plan Document.

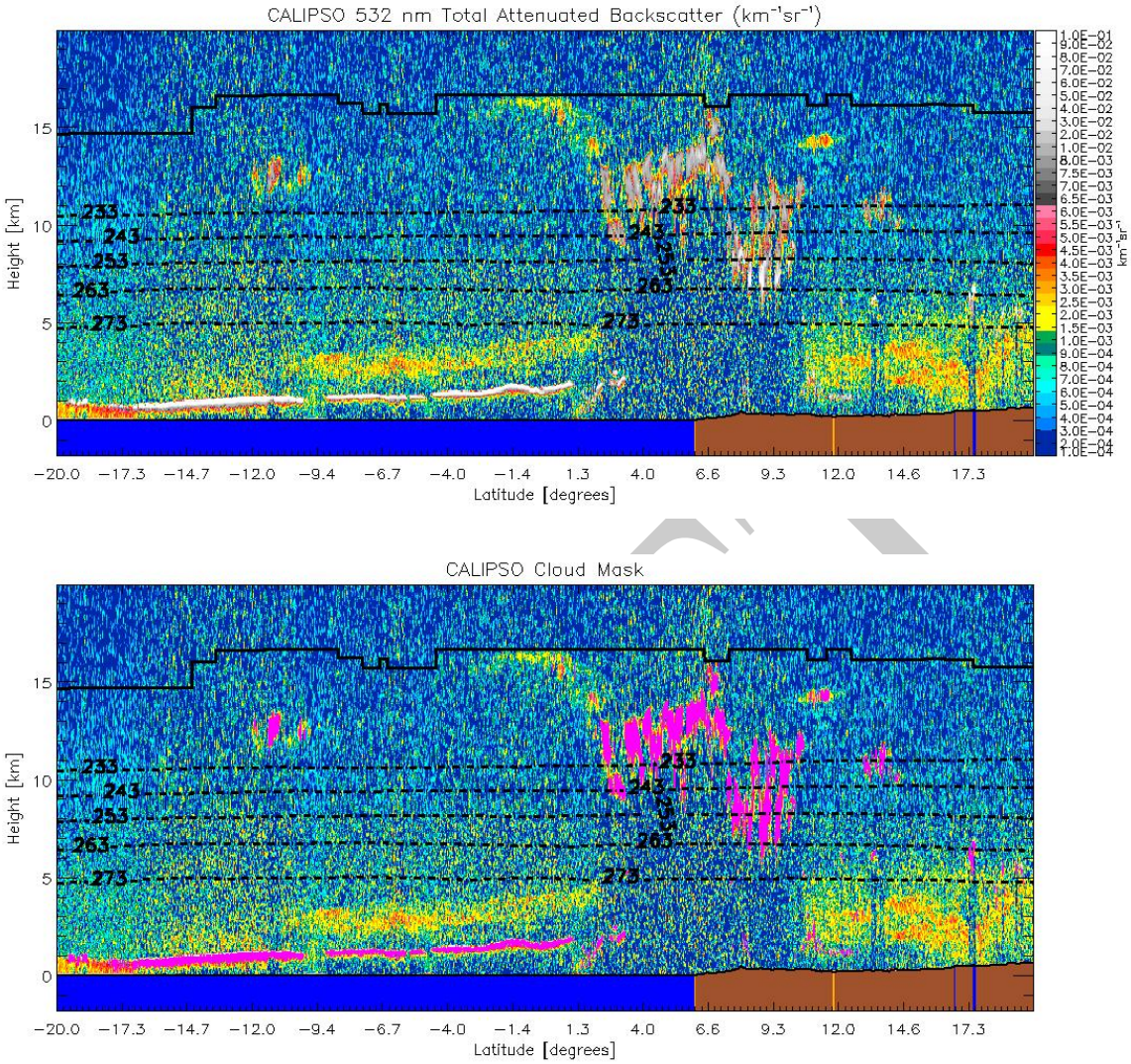

Figure 14: Illustration of the CALIOP data used in this study. Top image shows a 2d backscatter profile. Bottom image shows the detected cloud layers overlaid onto the backscatter image. Cloud layers are color magenta

4.2 Output from Simulated/Proxy Inputs Data Sets

The ABI-VAA has been tested on numerous volcanic ash eruptions within the SEVIRI domain. An example of the ABI ash cloud height and mass-loading products (along with the effective particle radius) is shown for the eruption of Eyjafjallajokull on May 6, 2010 (12:00 UTC) in Figure 15.

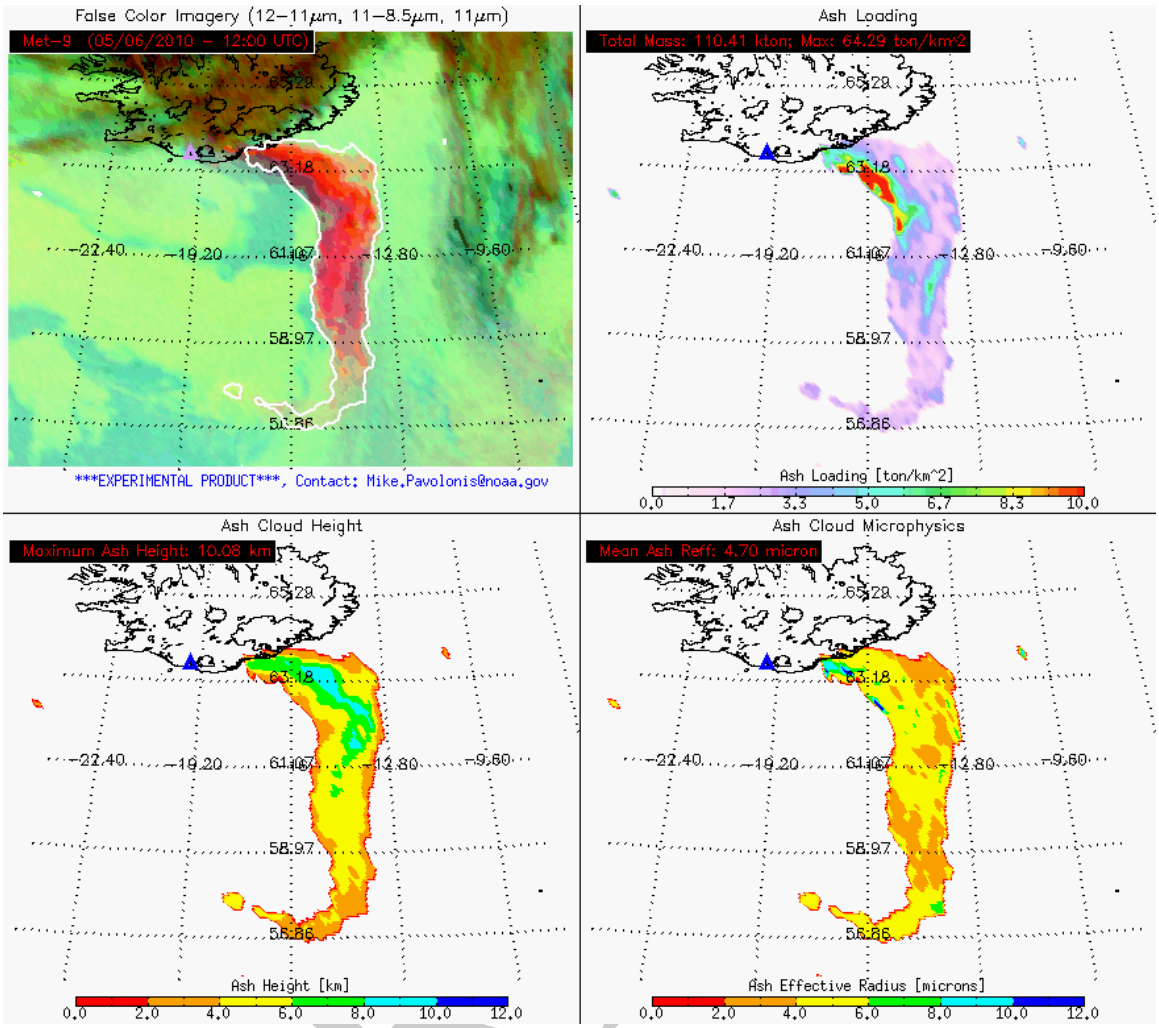

Figure 15: The ABI volcanic ash products were generated for an eruption of Eyjafjallajokull captured by SEVIRI on May 6, 2010 at 12:00 UTC. The volcanic ash cloud appears magenta in the false color image (top, left panel). The ash cloud height is shown in the bottom, left panel, the ash mass loading is shown in the top, right panel, and the effective particle radius in the bottom, right panel.

4.2.1 Precisions and Accuracy Estimates

The GOES-R ABI (and JPSS VIIRS) volcanic ash requirements are expressed such that the vertical resolution is 3-km and the measurement accuracy and precision are 2.0 and 2.5 tons/km^2, respectively. The accuracy and precision thresholds obviously apply to the ash mass loading. We interpret the 3-km vertical resolution as the accuracy (bias) threshold for the volcanic ash cloud top height. Several different validation procedures are utilized.

Routine validation of the volcanic ash products is challenging given that volcanic ash clouds are infrequently measured by active ground-based sensors or even by active

spaceborne sensors such as the CALIOP. Targeted in-situ measurements do not exist since it is considered highly dangerous to fly manned aircraft into volcanic ash clouds. Our general validation plan is to supplement the relatively infrequent spaceborne lidar observations of volcanic ash clouds with comparisons to ash products derived from instruments that are more sensitive to volcanic ash than the ABI. We will also employ vicarious validation techniques, where we apply the volcanic ash retrieval algorithm to other types of clouds that are commonly observed. Manual analysis can also be used to some extent.

Given the lack of direct measurements of volcanic ash clouds, truth is very difficult to define. Based on the validation that has been performed thus far, and the fact that this retrieval methodology has been applied successfully to meteorological clouds, the ABI volcanic ash products are expected to meet specification, relative to imperfect validation sources.

4.2.2 Error Budget

In the following sections, three different validation techniques (null validation, vicarious validation, and direct validation) are applied to the GOES-R volcanic ash products.

4.2.2.1 Validation of the Null Case

In the absence of a volcanic ash cloud, the retrieved ash mass loading should be 0 tons/km^2. This is referred to as the null case. *A posteriori* it well known which SEVIRI full disk scenes do not contain volcanic ash clouds, based on eruption records. Thus, a random sampling of SEVIRI full disk scenes, void of volcanic ash, can be used to quantify the retrieval error under these conditions. This sort of validation is important since a low ash detection false alarm rate is critical to users. Each full disk contains 1x10^7 pixels. The mean accuracy and precision (using 0.0 tons/km^2 as truth) are 0.033 tons/km^2 and 0.404 tons/km^2, respectively. The accuracy and precision for each of the 8 SEVIRI full disks are shown in Table 29. All of these values are well within the mass loading accuracy and precision specifications.

Table 29: The accuracy and precision of the ash mass loading product when applied to 8 SEVIRI full disks that were void of volcanic ash and dust. In this null case, the true value is 0.0 tons/km^2.

Scene	Accuracy (tons/km^2)	Precision (tons/km^2)
January 1, 2008, 00 UTC	0.027	0.340
January 1, 2008, 12 UTC	0.007	0.245
April 1, 2008, 00 UTC	0.015	0.237
April 1, 2008, 12 UTC	0.008	0.211
July 7, 2008, 00 UTC	0.074	0.510
July 7, 2008, 12 UTC	0.023	0.243
October 14, 2008, 00 UTC	0.069	0.821

October 14, 2008, 12 UTC	0.042	0.630
Mean	0.033	0.404

4.2.2.1.1 Validation of the Null Case – JPSS/VIIRS

This subsection supplements the parent subsection, with validation of the null case for JPSS/VIIRS observations given in Table 30. The mean accuracy and precision (using 0.0 tons/km^2 as truth) are 0.036 ton/km^2 and 0.364 tons/km^2, respectively (total pixels for the 4 swathes was 9.568 x 10^7). All these values are well within the mass loading accuracy and precision specifications.

Table 30: The accuracy and precision of the ash mass loading product when applied to VIIRS swathes that were void of volcanic ash and dust. In this null case, the true value is 0.0 tons/km^2. Total pixels were 9.568 x 10^7.

Scene	Accuracy (tons/km^2)	Precision (tons/km^2)
Sept. 22, 2015 0456 - 0511 UTC	0.009	0.179
Sept. 22, 2015 0716 - 0730 UTC	0.045	0.381
Feb. 22, 2015 0434 - 0447 UTC	0.006	0.144
Feb. 22, 2015 0830 - 0846 UTC	0.081	0.731
Mean	0.036	0.364

4.2.2.2 Vicarious Validation

The volcanic ash retrieval described in this ATBD can be applied to meteorological clouds using modified cloud microphysical assumptions. CALIOP observations of meteorological clouds are very common, so a statistically significant validation analysis of meteorological clouds is possible. As shown in the ABI Cloud Height ATBD, the meteorological cloud height accuracy is well within the 3 km ash cloud specification, which gives confidence that the ash cloud heights will also be within the specification.

While the meteorological cloud analysis adds confidence, it is limited by the fact that volcanic ash clouds exhibit a very different spectral signature in the infrared. Applying the GOES-R ash retrieval to dust clouds can largely negate this limitation. Dust clouds, which are frequently observed by CALIOP, have a very similar spectral signature as ash clouds in the infrared (stronger absorption near 11 μm than at 12 and 13.3 μm). The GOES-R ash retrieval algorithm was applied to several airborne dust cases observed by CALIOP and MODIS, totaling 3,432 co-located pixels. It is straightforward to compare the cloud height retrieved by the GOES-R algorithm and the CALIOP-derived cloud top height, as is shown in Figure 16. The GOES-R heights fall within the dust cloud layer as depicted by the CALIOP 532 nm total attenuated backscatter. As expected, the GOES-R heights are biased low (Bias = -1.43 km, see Table 31) relative to the top boundary of the

dust layers since the infrared measurements are sensitive to an extinction-weighted cloud temperature, not the cloud top temperature.

The mass-loading product can also be validated using CALIOP. The CALIOP vertical cloud boundary information along with a co-located temperature profile (from NWP) can be used to determine a high quality effective cloud temperature estimate. Given the effective cloud temperature and estimates of the clear sky radiance, a "truth" cloud emissivity can be calculated for a give spectral channel. The "truth" 11-μm cloud emissivity and the "truth" β(12/11μm) can then be used to compute the mass loading using the procedure described in Sections 3.4.3.2 and 3.4.4.6. The major weakness of this procedure is that the microphysical assumptions used in converting the 11-μm cloud emissivity and the β(12/11μm) to mass loading cannot be validated. These assumptions can only be validated using in-situ measurements of ash clouds, which do not exist at this point. Table 31 shows that the retrieved mass loading agrees well with the mass loading calculated using the CALIOP vertical cloud boundaries. The accuracy and precision are 0.40 tons/km^2 and 1.03 tons/km^2, respectively. Both are well within the F&PS specifications.

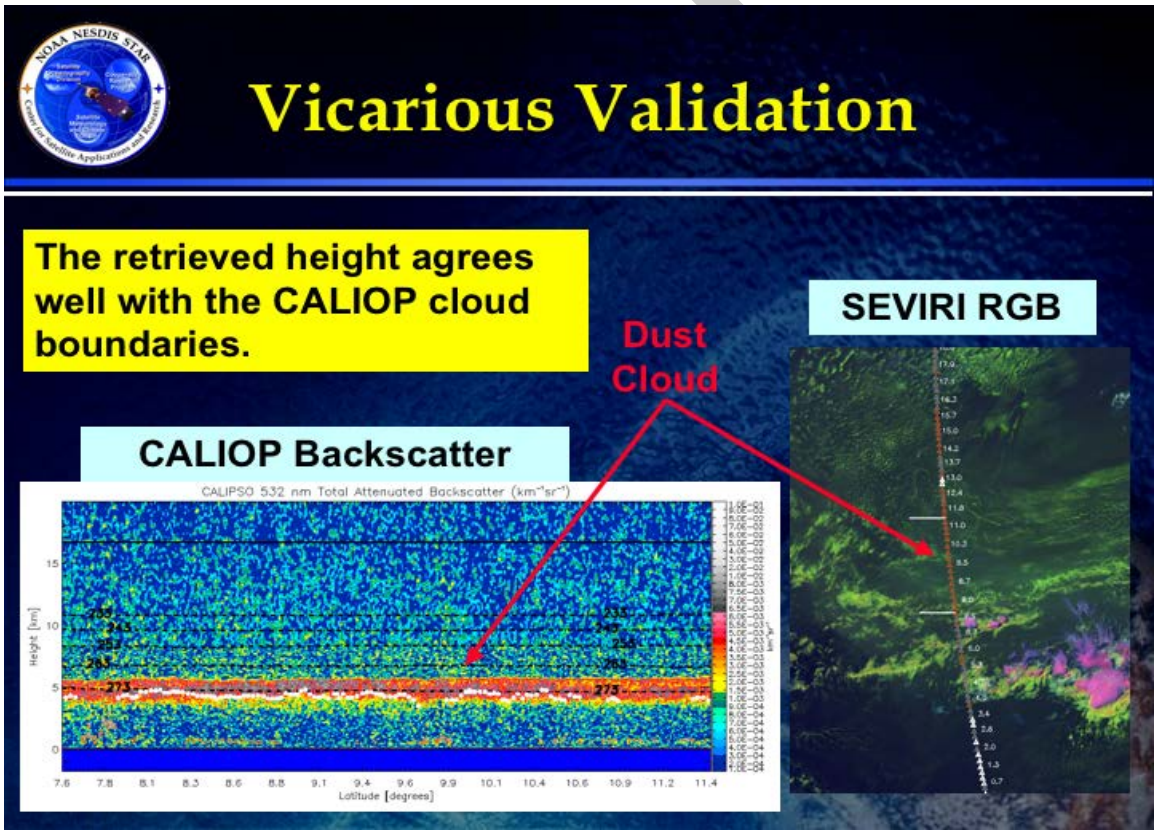

Figure 16: The GOES-R volcanic ash retrieval algorithm was applied to an elevated Saharan dust cloud, which exhibits a spectral signature that is very similar to ash in the infrared. The results of the height retrieval algorithm are overlaid (white

circles) on a 532 nm CALIOP total attenuated backscatter cross section. The retrieval results agree well with the lidar positioning of the dust cloud.

Product	Bias	Accuracy (absolute value of bias)	Precision (stddev of bias)
Ash Top Height	-1.43 km	1.43 km	1.49 km
Ash Mass Loading	0.40 tons/km^2	0.40 tons/km^2	1.03 tons/km^2

Table 31: Accuracy (mean bias) and precision (standard deviation of bias) statistics derived from comparisons between CALIOP derived dust cloud top heights and mass loading and those retrieved using the GOES-R volcanic ash algorithm for 3,432 match-ups.

4.2.2.3 CALIOP Observations of Ash Clouds

CALIOP observations of ash clouds are rare, but as CALIOP service time increases, the amount of co-located ash observations increases. Recent eruptions of Eyjafjallajokull, Soufriere Hills, Alaskan Volcanoes and other volcanoes have provided many additional match-ups to the existing database. The increased number of volcanic ash cases viewed by CALIOP and SEVIRI/MODIS allows for a more significant ash validation (although still small compared to amount of dust match-ups). The GOES-R ash retrieval algorithm was applied to several airborne volcanic ash cases observed by CALIOP and MODIS, totaling 434 co-located pixels. The height and mass loading validation of ash clouds follows the same process illustrated with dust clouds (section 4.2.2.2). The GOES-R heights are biased low (Bias = -0.74km, see Table 32) relative to the top boundary of the ash clouds. Table 32 shows the mass loading agrees well with the mass loading calculated using the CALIOP vertical cloud boundaries. The accuracy and precision are 0.58 tons/km^2 and 1.95 tons/km^2, respectively. Both are well within the F&PS specifications.

Product	Bias	Accuracy (absolute value of bias)	Precision (stddev of bias)
Ash Top Height	-0.74 km	0.74 km	2.24 km
Ash Mass Loading	0.58 tons/km^2	0.58 tons/km^2	1.95 tons/km^2

Table 32: Accuracy (mean bias) and precision (standard deviation of bias) statistics derived from comparisons between CALIOP derived ash cloud top heights and mass loading and those retrieved using the GOES-R volcanic ash algorithm for 434 CALIOP/MODIS match-ups.

The total accuracy and precisions statistics for all co-located dust and ash scenes is given in Table 33.

Product	Bias	Accuracy (absolute value of bias)	Precision (stddev of bias)

Ash Top Height	-1.35 km	1.35 km	1.95 km
Ash Mass Loading	0.42 tons/km^2	0.42 tons/km^2	1.17 tons/km^2

Table 33: Accuracy (mean bias) and precision (standard deviation of bias) statistics derived from comparisons between CALIOP derived dust and ash cloud top heights and mass loading and those retrieved using the GOES-R volcanic ash algorithm for 3,866 CALIOP/MODIS match-ups.

4.2.3 Validation for JPSS/VIIRS

This subsection was added for discussion related to JPSS/VIIRS validation. Identical concepts outlined in sections 4.2.2.2 and 4.2.2.3 can be used to validate the VIIRS-VAA algorithm output, **however VIIRS/CALIOP co-locations with volcanic ash present are exceptionally rare** (this is true because volcanic ash is rare and even more so because VIIRS and CALIOP orbits seldom overlap). To validate a sufficient number of volcanic ash pixels, we utilize MODIS/CALIOP validation results (using MODIS channels only available from VIIRS). To motivate the validity of such a concept, it is beneficial to utilize when MODIS and VIIRS view an ash cloud very close in both space and time. The results of the VIIRS-VAA algorithm run with 1) VIIRS observations and 2) MODIS observations (using only channels available from VIIRS) are shown for an eruption of Raung Volcano in Indonesia from July 25, 2015 (Figure 17). The differences between the two are small and the ash height scatter plot indicates the results agree well.

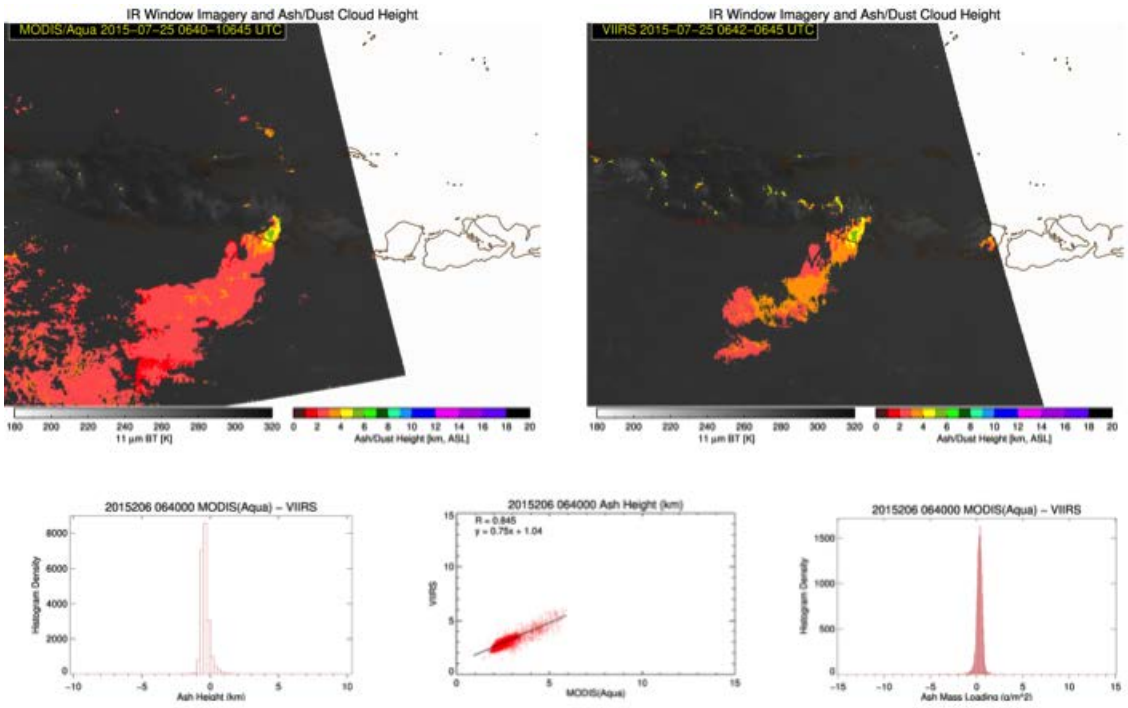

Figure 17: VIIRS-VAA ash height output using MODIS (top left) and VIIRS (top right) for the Raung volcano 0640-0645 UTC 25 July 2015. Only channels available from VIIRS are used in the MODIS output. The bottom panels from left to right show ash heightx difference, ash height scatter plot, and ash mass loading difference.

The VIIRS-VAA applied to MODIS (using only VIIRS channels) and using CALIOP as truth shows the VIIRS-VAA is well within specifications for ash cloud height and ash mass loading. The total accuracy and precision statistics are given in Table 34 for all co-located ash and dust scenes described in sections 4.2.2.2 and 4.2.2.3.

Product	Bias	Accuracy (absolute value of bias)	Precision (stddev of bias)
Ash Top Height	-1.91 km	1.91 km	1.37 km
Ash Mass Loading	1.13 tons/km^2	1.13 tons/km^2	1.40 tons/km^2

Table 34: Accuracy (mean bias) and precision (standard deviation of bias) statistics derived from comparisons between CALIOP derived dust and ash cloud top heights and mass loading and those retrieved using the VIIRS-VAA for 3,866 CALIOP/MODIS match-ups (applied to only VIIRS channels).

4.2.4 Validation Summary

The following points summarize the results of the volcanic ash validation analysis.

- According to the F&PS, the volcanic ash cloud top height has an accuracy requirement of 3 km and the mass loading has an accuracy and precision requirement of 2 tons/km^2 and 2.5 tons/km^2, respectively.

- Spaceborne lidar observations of ash clouds and dust clouds (which are spectrally similar to ash clouds in the channels used by the ABI-VAA) were used as validation sources.

- The comparisons to both ash and dust clouds indicates that the ABI-VAA has a cloud height accuracy of 1.35 km, and the mass loading has an accuracy and precision of 0.42 tons/km^2 and 1.17 tons/km^2, respectively. Thus, the ABI VAA products meet the F&PS accuracy specifications.

- The comparisons to both ash and dust clouds indicates that the VIIRS-VAA has a cloud height accuracy of 1.91 km, and the mass loading has an accuracy and precision of 1.13 tons/km^2 and 1.40 tons/km^2, respectively. Thus, the VIIRS-VAA products meet the accuracy specifications.

5 PRACTICAL CONSIDERATIONS

5.1 Numerical Computation Considerations

The ABI-VAA employs an optimal estimation framework. Therefore it requires inversions of matrices that can under severe scenarios become ill-conditioned. Currently, these events are detected and treated as failed retrievals. In addition, the matrices have small dimensions. Thus, operations on them are not computationally expensive. In addition, prior to converting cloud emissivity to optical depth, the cloud emissivity must be checked to ensure that it is greater than 0.0 and less than 1.0 to prevent an illegal natural logarithm operation.

5.2 Programming and Procedural Considerations

The ABI-VAA makes heavy use of clear-sky radiative transfer calculations. Our current system computes the clear-sky atmospheric transmittances at low spatial resolution and with enough angular resolution to capture sub-grid variation path-length changes. This step is critical, as performing clear-sky atmospheric transmittance calculations for each pixel requires extensive memory and CPU time, but does not produce significantly better scientific results. The AIADD Document describes this procedure in detail.

NWP data is heavily utilized in the ABI Volcanic Ash Algorithm. The algorithm can tolerate the use NWP data for forecasts ranging from 0 to 24 hours.

The ABI-VAA can provide usable results out to a viewing angle of 80 degrees (the F&PS minimum requirement is 60 degrees). The ABI-VAA is not applied to pixels that have a viewing angle greater than 80 degrees (the ash height and mass loading are set to missing in this case and ash confidence is set to "not-ash").

5.3 Quality Assessment and Diagnostics

The optimal estimation framework provides automatic diagnostic metrics and estimates of the retrieval error. We recommend that the error covariance matrices be monitored on at least a monthly basis. We also believe that the validation techniques described earlier, and in the ABI Volcanic Ash Product Validation Plan, be implemented on a regular basis.

5.4 Exception Handling

Prior to use, the ABI-VAA checks to make sure that each channel falls within the expected measurement range and that valid clear sky radiance and transmittance profiles are available for each channel. The ABI-VAA is only applied to a given pixel if all channels used in the algorithm contain valid data (according to the L1b calibration flags); otherwise the algorithm output is flagged as missing. The science of the volcanic ash algorithms does not allow for a graceful degradation of the products. The algorithm, however, can tolerate the use NWP data for forecasts ranging from 0 to 24 hours.

5.5 Algorithm Validation

Volcanic ash clouds are present infrequently relative to other types of cloud, and lidars and in-situ instruments rarely observe them. As such, volcanic ash products are very difficult to validate. Despite this challenge, it is currently possible to use spaceborne lidar observations (CALIOP) of volcanic ash and desert dust to validate the ABI volcanic ash algorithm as applied to SEVIRI or MODIS. While quite rare, any future matchups of VIIRS and CALIOP observations of volcanic ash will be used to validate the VIIRS-VAA. During the GOES-R era though, it is not guaranteed that spaceborne lidar observations of ash or dust, co-located with ABI measurements, will be available, although the European Space Agency (ESA) EarthCARE mission is scheduled to coincide with the GOES-R era. The availability of spaceborne lidar observations during the GOES-R era should only pose a moderate risk to the validation of the ABI volcanic

ash algorithm because the algorithm was designed to be minimally sensitive to the exact characteristics of the channels used in the algorithm. The algorithm is sensitive, however, to the accuracy of the ABI clear sky radiance calculations that are needed. Thus, one of our main focuses will be to monitor the clear sky radiance biases during ABI operations, especially early on. Finally, we are hopeful that in-situ observations via UAV's will be possible during the GOES-R era, as in-situ measurements are the ultimate direct validation source. Continued collaboration with the volcanic ash research community is critical to assure access to unique and detailed validation data sets. Please refer to the ABI Volcanic Ash Product Validation Plan Document for extensive information on pre and post launch validation plans.

6 ASSUMPTIONS AND LIMITATIONS

The following sections describe the current limitations and assumptions in the current version of the ABI-VAA

6.1 Performance

The following assumptions have been made in developing and estimating the performance of the ABI-VAA. The following lists contain the current assumptions and proposed mitigation strategies.

1. NWP data of comparable or superior quality to the current 6 hourly GFS forecasts are available. (Mitigation: Use longer-range GFS forecasts or switch to another NWP source – e.g. ECMWF).

2. Top-of-atmosphere clear sky radiances are available for each pixel and 101 level profiles of clear sky atmospheric transmittance and radiance are available at the NWP data horizontal resolution. (Mitigation: Use reduced spatial resolution top-of-atmosphere clear sky radiances. The profiles of transmittance and radiance must be present at, at least, the NWP spatial resolution and 101 vertical levels).

3. All of the static ancillary data are available at the pixel level. (Mitigation: Reduce the spatial resolution of the surface type, land/sea mask and or coast mask).

4. The processing system allows for processing of multiple scan lines at once for application of important spatial analysis techniques. (Mitigation: No mitigation is possible).

5. All ABI channels required (see Table 3: Channel numbers and wavelengths for the ABI) by the algorithm must be available. (Mitigation: Develop a

modified version of the algorithm. Graceful degradation is not possible because there are too many possible channel permutations.).

In addition, the clear sky radiance calculations are prone to large errors, especially near coastlines, in mountainous regions, snow/ice field edges, and atmospheric frontal zones, where the NWP surface temperature and atmospheric profiles are less accurate. The impact of these errors on the ABI-VAA depends on the cloud optical depth. For optically thick clouds (infrared optical depth of about 1.0 or greater), these errors have a small impact since the difference between the observed and black cloud radiance approach zero as the cloud optical depth increases. This is not the case for optically thin clouds, where inaccurate NWP data can have serious impacts. Thus, clear sky radiance biases need to be monitored on a regular basis (~monthly).

6.2 Assumed Sensor Performance

We assume the sensor will meet its current specifications. However, the ABI-VAA will be dependent on the following instrumental characteristics.

- Unknown spectral shifts in some channels will cause biases in the clear-sky RTM calculations that may impact the performance of the ABI-VAA. Clear sky radiance biases need to be monitored throughout ABI's lifetime.

6.3 Pre-Planned Improvements

We expect in the coming years to focus on the following improvement.

6.3.1 Use of 10.4-μm channel

The 10.4 μm channel is new to the world of satellite imagers. Large variations in cloud emissivity occur in the 10 – 13 μm spectral range. With the 10.4 μm channel additional cloud emissivity relationships can be exploited in detecting volcanic ash and determining its microphysical properties. We expect the GOES-R Risk Reduction projects to demonstrate its use before implementation into the operational algorithm.

7 REFERENCES

Cox, S. K., 1976: Observations of Cloud Infrared Effective Emissivity. *J.Atmos.Sci.,* **33**, 287-289.

Downing, H. D., D. Williams, 1975: Optical-Constants of Water in Infrared. *Journal of Geophysical Research*, **80**, 1656-1661.

Giraud, V., J. C. Buriez, Y. Fouquart, F. Parol, and G. Seze, 1997: Large-scale analysis of cirrus clouds from AVHRR data: Assessment of both a microphysical index and the cloud-top temperature. *J.Appl.Meteorol.,* **36**, 664-675.

Hansen, M., R. DeFries, J.R.G. Townshend, and R. Sohlberg (1998), UMD Global Land Cover Classification, 1 Kilometer, 1.0, Department of Geography, University of Maryland, College Park, Maryland, 1981-1994.

Heidinger, A. K. and M. J. Pavolonis, 2009: Nearly 30 years of gazing at cirrus clouds through a split-window. Part I: Methodology. *J.Appl.Meteorol. and Climatology*, **48(6)**, 110-1116.

Inoue, T., 1987: A Cloud Type Classification with Noaa 7 Split-Window Measurements. *J.Geophys.Res.-Atmos.,* **92**, 3991-4000.

Mitchell, D. L., 2000: Parameterization of the Mie extinction and absorption coefficients for water clouds. *J.Atmos.Sci.,* **57**, 1311-1326.

Neal, C. A., R. G. McGimsey, C. A. Gardner, M. L. Harbin, and C. J. Nye, 1994: Tephra-fall deposits from 1992 eruptions of Crater Peak, Mount Spurr Volcano, AK: A preliminary report on distribution, stratigraphy, and composition. The 1992 eruptions of Crater Peak vent, Mount Spurr volcano, Alaska, U.S. Geological Survey Bulletin 2139, 65-79.

Parol, F., J. C. Buriez, G. Brogniez, and Y. Fouquart, 1991: Information-Content of Avhrr Channels 4 and 5 with Respect to the Effective Radius of Cirrus Cloud Particles. *J.Appl.Meteorol.,* **30**, 973-984.

Pavolonis, M. J., A. K. Heidinger, 2004: Daytime cloud overlap detection from AVHRR and VIIRS. *J.Appl.Meteorol.,* **43**, 762-778.

Pavolonis, M. J., W. F. Feltz, A. K. Heidinger, and G. M. Gallina, 2006: A daytime complement to the reverse absorption technique for improved automated detection of volcanic ash. *J.Atmos.Ocean.Technol.,* **23**, 1422-1444.

Pavolonis, M. J., 2010: Advances in extracting cloud composition information from spaceborne infrared radiances: A robust alternative to brightness temperatures. Part I: Theory. *J. Applied Meteorology and Climatology,* **49**, 1992-2012.

Pavolonis, M. J., 2010b: Advances in extracting cloud composition information from spaceborne infrared radiances: A robust alternative to brightness temperatures. Part II: Proof of concept. To be submitted to *J. Applied Meteorology and Climatology*.

Pollack, J. B., O. B. Toon, and B. N. Khare, 1973: Optical Properties of some Terrestrial Rocks and Glasses. *Icarus,* **19**, 372-389.

Prata, A. J., 1989: Observations of volcanic ash clouds in the 10-12-micron window using AVHRR/2 Data. *Int.J.Remote Sens.,* **10**, 751-761.

Prata, A. J. and I. F. Grant, 2001: Retrieval of microphysical and morphological properties of volcanic ash plumes from satellite data: Application to Mt Ruapehu, New Zealand. *Q. J. R. Meteorol. Soc.*, **127**, 2153-2179.

Rodgers, C. D., 1976: Retrieval of atmospheric temperature and composition from remote measurements of thermal radiation. *Reviews of Geophysics and Space Physics*, **14**, 609-+.

Roush, T., J. Pollack, and J. Orenberg, 1991: Derivation of Midinfrared (5-25 Mu-M) Optical-Constants of some Silicates and Palagonite. *Icarus*, **94**, 191-208.

Turner, D. D., 2005: Arctic mixed-phase cloud properties from AERI lidar observations: Algorithm and results from SHEBA. *J.Appl.Meteorol.*, **44**, 427-444.

Seemann, S. W., E. E. Borbas, R. O. Knuteson, G. R. Stephenson, and H. Huang, 2008: Development of a global infrared land surface emissivity database for application to clear sky sounding retrievals from multispectral satellite radiance measurements. *J.Appl.Meteorol.Climatol.,* **47**, 108-123, doi:10.1175/2007JAMC1590.1.

Van de Hulst, H. C., 1980: *Multiple Light Scattering, Tables, Formulas, and Applications.* Vol. 2. Academic Press, 739 pp.

Wen, S. and W. I. Rose, 1994: Retrieval of sizes and total masses of particles in volcanic ash clouds using AVHRR bands 4 and 5. *J. Geophys. Res.*, **99**, 5421-5431.

Warren, S. G., R. E. Brandt, 2008: Optical constants of ice from the ultraviolet to the microwave: A revised compilation. *J.Geophys.Res.-Atmos.*, **113**, D14220, doi:10.1029/2007JD009744.

Yang, P., H. L. Wei, H. L. Huang, B. A. Baum, Y. X. Hu, G. W. Kattawar, M. I. Mishchenko, and Q. Fu, 2005: Scattering and absorption property database for nonspherical ice particles in the near- through far-infrared spectral region. *Appl.Opt.,* **44**, 5512-5523.

Zhang, H., W. P. Menzel, 2002: Improvement in thin cirrus retrievals using an emissivity-adjusted CO2 slicing algorithm. *J.Geophys.Res.-Atmos.*, **107**, 4327, doi:10.1029/2001JD001037.

Zhang, P., N. Lu, X. Hu, and C. Dong, 2006: Identification and physical retrieval of dust storm using three MODIS thermal IR channels. *Global Planet.Change*, **52**, 197-206, doi:10.1016/j.gloplacha.2006.02.014.